JGR Planets

RESEARCH ARTICLE

10.1029/2024JE008728

A Search for the Near-Surface Particulate Layer Using Venera 13 In Situ Spectroscopic Observations

Shubham V. Kulkarni[1], Patrick G. J. Irwin[1], Colin F. Wilson[1,2], and Nikolai I. Ignatiev[3]

[1]Department of Physics, University of Oxford, Oxford, UK, [2]ESA—European Space Research and Technology Centre (ESTEC), Noordwijk, The Netherlands, [3]Space Research Institute (IKI), Russian Academy of Sciences, Moscow, Russia

Abstract Whether or not there is a particulate layer in the lowest 10 km of the Venusian atmosphere is still an open question. Some of the past in situ experiments showed the presence of a detached particulate layer, and a few suggested the existence of finely dispersed aerosols, while other instruments supported the idea of no particulate matter in the deep atmosphere. In this work, we investigate the presence of a near-surface particulate layer (NSPL) using in situ data from the Venera 13 mission. While the original spectrophotometric data from Venera 13 were lost, we have reconstructed a part of this data by digitizing the old graphic material and selected the eight most reliable Venera 13 downward radiance profiles from 0.48 to 0.8 μm for our retrievals. The retrievals suggest the existence of the particulate layer with a peak in the altitude range of 3.5–5 km. They further indicate a log-normal particle size distribution with a mean radius between 0.6 and 0.85 μm. The retrievals constrain the real refractive index of the particles to lie around the range of 1.4–1.6, with the imaginary refractive index of a magnitude of 10^{-3}. Based on refractive index retrievals, uplifted basalt particles or volcanic ash could be responsible for near-surface particulates. In comparison, volatile condensates appear less likely to be behind the formation of NSPL.

Plain Language Summary Several in situ missions have visited Venus in the past. However, the extreme conditions in the deep atmosphere created difficulty with in situ measurements. Hence, inconsistent evidence is available regarding the existence of particulate matter in the deepest part of the atmosphere. To investigate the presence of particulates, we have reconstructed the spectra measured from an altitude of 62 km in the atmosphere to the surface by the Venera 13 Lander. Our analysis strongly suggests the presence of a particulate layer approximately 3.5–5 km above the surface. The analysis further indicates two possible formation mechanisms. The first mechanism proposes that the particulates could be basaltic dust uplifted from the surface, as the Venusian surface is largely made of basalt and shows ample evidence of wind-driven transport. The second mechanism suggests that volcanic ash might be the source of the particles, given the large number of Volcanic orifices on the surface and the possibility of active volcanism.

Key Points:

- Reanalysis of Venera 13 spectrophotometric data strongly suggests the existence of a near-surface particulate layer in the atmosphere
- The layer appears to be made up of submicron-sized particles and peaks between the altitude of 3.5–5 km above the surface
- The optical properties of the particles are consistent with basaltic dust and volcanic ash

Correspondence to:

S. V. Kulkarni,
shubham.kulkarni@physics.ox.ac.uk

Citation:

Kulkarni, S. V., Irwin, P. G. J., Wilson, C. F., & Ignatiev, N. I. (2025). A search for the near-surface particulate layer using Venera 13 in situ spectroscopic observations. *Journal of Geophysical Research: Planets*, *130*, e2024JE008728. https://doi.org/10.1029/2024JE008728

Received 12 SEP 2024
Accepted 27 MAR 2025

Author Contributions:

Conceptualization: Patrick G. J. Irwin, Colin F. Wilson
Data curation: Shubham V. Kulkarni, Nikolai I. Ignatiev
Formal analysis: Shubham V. Kulkarni
Funding acquisition: Patrick G. J. Irwin, Colin F. Wilson
Investigation: Shubham V. Kulkarni
Methodology: Shubham V. Kulkarni, Patrick G. J. Irwin, Colin F. Wilson
Project administration: Patrick G. J. Irwin, Colin F. Wilson
Resources: Shubham V. Kulkarni, Patrick G. J. Irwin, Colin F. Wilson, Nikolai I. Ignatiev
Software: Shubham V. Kulkarni, Patrick G. J. Irwin, Colin F. Wilson
Supervision: Patrick G. J. Irwin, Colin F. Wilson
Validation: Shubham V. Kulkarni, Patrick G. J. Irwin, Colin F. Wilson
Visualization: Shubham V. Kulkarni

1. Introduction

Venus has a continuous global cloud cover along with a dense atmosphere which is optically thick at visible wavelengths. This complicates the sounding of the deep atmosphere from remote sensing observations (Titov et al., 2018). Thus, before the discovery of near-IR spectroscopic windows on the dark side of Venus (Allen & Crawford, 1984), Venus exploration focused particularly on in situ observations. In 1967, Venera 4 became the first probe to perform in situ measurements of a planet's atmosphere other than Earth. Since then, there have been 17 successful in situ lander missions, the last of which was the Vega-2 lander in 1984. These in situ missions provided a plethora of measurements in the atmosphere that forms the basis of the current understanding of the Venusian deep atmosphere (O'Rourke et al., 2023).

In spite of the series of in situ missions, the deepest part of the atmosphere still remains a mysterious place. On 9 December 1978, four Pioneer Venus (PV) probes landed simultaneously on Venus. The PV "North" and "Night" probes landed on the night side at coordinates (59.3°N, 4.8°E) and (28.7°S, 56.7°E), respectively. The Nephelometer onboard both probes showed a small isolated increase in the backscattering cross-sections centered at an altitude of 4.6 and 3.8 km with respect to a planetary radius of 6,052 km (Ragent & Blamont, 1980). This was the only signal recorded below 30 km on both probes and thus forms the first indication of a detached near-surface particulate layer (NSPL). Whereas on the day side, the PV "Large" and "Day" probes landed at coordinates (4.4°N, 304.0°E) and (31.3°S, 317.0°E), respectively. The Nephelometers onboard both probes did not detect any

Writing – original draft: Shubham V. Kulkarni
Writing – review & editing: Shubham V. Kulkarni, Patrick G. J. Irwin, Colin F. Wilson, Nikolai I. Ignatiev

backscattering signals below an altitude of 30 km. However, the background radiometric channel in the Nephelometer on board the Large probe detected fluctuations, particularly below 8 km. As noted by Ragent and Blamont (1980), these fluctuations could have been caused by the probe motion or by the presence of particulate matter too far from the probe to have been detected by the backscatter channel, but within the field of view of the radiometric channel of the Nephelometer. Similarly, while analyzing the Large Probe Cloud Particle Size Spectrometer (LCPS) data, Knollenberg and Hunten (1980) noted the presence of noise bursts near the surface that could have masked real particle events. They also mentioned that the existence of particles larger than 2 μm could still be discounted despite the noise.

A few days later, on 25 December 1978, the Venera 11 probe landed on the dayside of Venus at (14°S, 299°E). The backscattering Nephelometer detected a signal from 12 to 8 km, but no signals were detected below 8 km (Marov et al., 1979). Subsequently, the Venera 13 and 14 probes plunged into the atmosphere of Venus on 1 March and 5 March 1982. The probes landed on dayside at coordinates (7.5°S, 303°E) and (13.25°S 310°E) which are ≈950 km apart from each other. It was reported that the Nephelometer signal on both probes showed an irregular character from an altitude of 19 km down to the surface. However, the signal could have been affected by the presence of instrumental effects due to the heating of the thermal insulation of the Nephelometer and it was difficult to discern the contamination from the actual signal (Marov et al., 1983). Apart from the Nephelometers, the Venera probes also carried dedicated spectrophotometers since the Venera 8 mission in 1972. The earlier interpretations of the spectrophotometric data from Venera 8 to 14 missions recorded a deviation in the observed scattering coefficient of up to 30% from the Rayleigh scattering coefficient. However, they generally favored the idea of the atmosphere below 10 km being clear of large particles (Avduevsky et al., 1973; Ekonomov et al., 1979; I. M. Golovin & Ustinov, 1982; Moshkin et al., 1983). The analysis of a reconstructed Venera 11, 13, and 14 spectrophotometric data by Dlugach (1988) showed the presence of fine aerosols in the atmosphere below 32 km to the surface. More recently, the reanalysis of this data by Grieger et al. (2004) showed an increase in extinction indicating the presence of the NSPL with a peak altitude between 1 and 2 km above both the landing sites.

The pressure and temperature increase from 41 bar and 643 K, respectively, at 12 km, to 92 Bar and 735 K at the surface. Due to these extreme conditions, many optical instruments on the in situ probes either showed heavy contamination in the data or failed in the deep atmosphere. The solar flux radiometer (SNFR) on board all three Pioneer Venus Small probes anomalously failed at an altitude of 12.5 km in the atmosphere (Suomi et al., 1979). The background radiometric channels of the Nephelometer instrument on all four Pioneer Venus probes had a near-IR leak that resulted in complications for the absolute calibration of the data (Ragent et al., 1980). While the Venera 8 to 14 missions provided spectrophotometric data from about 60 km altitude down to the surface, the original data sets were lost and only the reconstructed version of a part of the data sets from Venera 11, 13, and 14 missions are still available (N. I. Ignatiev et al., 1997). Thus, the instrumental failures and contamination in the data due to extreme conditions along with the loss of original data could have partially prevented a consistent detection of the near-surface particulate layer.

The presence of such a layer would raise questions about the atmospheric or surface processes behind its formation. Most importantly, it could directly affect the surface imaging and spectroscopic observations from upcoming in situ missions, such as DAVINCI (Garvin et al., 2022) or a future balloon mission (Cutts et al., 2022), and orbiter missions like VERITAS (S. Smrekar et al., 2020) or EnVision (Straume-Lindner et al., 2022). Given the onset of these missions, we have reanalyzed the reconstructed Venera 13 data set using modern radiative transfer analysis methods to examine the presence of a near-surface particulate layer and to consider the extent to which the properties of the NSPL can be constrained.

2. Venera 13 and 14 In Situ Spectrophotometric Observations

The Venera 13 and 14 descent probes were equipped with a spectrophotometric complex known as IOAV-2. The instrument included three parts: a scanning spectrometer, a wide-angle spectrometer, and an ultraviolet photometer. The scanning spectrometer recorded radiation from two bands—(a) Visible $\lambda = 0.45$–0.7 μm, and (b) Near-IR $\lambda = 0.7$–1.2 μm. The FWHM of the filters in the Visible and near-IR bands were 25 and 22.2 nm, respectively. The scanning assembly allowed the radiation to be recorded from six different directions—1° (zenith), 44°, 130°, 159° (nadir), 230°, 316° with a field of view of 20°. Similarly, the wide-angle spectrometer, with its independent detector electronics, recorded the downward radiation from the entire upper hemisphere (i.e., with a field of view of ≈180°). It took 2.5 s to record one spectrum with ≈60 intensity values for the scanning

spectrometer (I_s) and ≈20 intensity values for the wide-angle spectrometer (I_w). The recorded signal from each of the detectors was passed on to two identical systems of signal converters (CK1 and CK2) that had different sensitivities and variable amplification coefficients. If the amplifier in either of the signal converters got saturated the amplification coefficient would switch to a lower value, providing a high dynamic range and sensitivity for signal conversion. A total of 1,500 such spectra were recorded by each probe from about 62 km altitude to the surface and for about half an hour on the surface after the landing.

The thermal protection of the scanning spectrometer and a wide-angle spectrometer was achieved in two stages. Each stage had elements that separately provided (a) thermal resistance and (b) heat capacity to maintain the inside temperature within the operational limits (Avduevskij et al., 1976). With this system, the temperature of the optoelectronic elements was maintained within the range of 305–310 K down to the surface (Moshkin et al., 1983) which allowed the instrument to function at outside temperatures of up to 800 K.

The UV photometer recorded the radiation in the wavelength range of 0.32–0.39 μm. The photometer used a scanning assembly mounted on the same axis as that of the scanning assembly used for the scanning spectrometer mentioned above. Using this mechanism, the UV photometer recorded the radiation from the six directions which are 6°, 45°, 132.5°, 164°, 227.5°, and 315° with a field of view of ≈4° (Ekonomov et al., 1983). The observations started at 62 km and were taken in sync and in phase with those of the scanning spectrophotometer. Unlike the scanning and the wide-angle spectrometers, the UV photometer was placed outside the thermally insulated pressurized compartment. Thus, the instrument was susceptible to atmospheric conditions and it was turned off at an altitude of ≈45 km when it reached the maximum operational temperature of ≈100°C.

The data transmitted back to Earth was recorded digitally on magnetic tapes (Sagdeev & Moroz, 1982). The data from the magnetic tapes were then processed at the Space Research Institute of the Russian Academy of Sciences (IKI) and during this period the spectrophotometric data was printed on graphs. In later years, attempts to read the data from magnetic tapes were unsuccessful. Thus, the original data were lost or became unreadable. Fortunately, some of the original graphic material regarding the data of the scanning spectrometer and the wide-angle spectrometer is still available and we have digitized a part of it to reconstruct the data set. Unfortunately, any substantial graphic material involving the UV photometer data could not be found and hence it was not digitized. The reconstructed data set provides the data products in three formats as explained next.

2.1. Format 0 Data Products

The original graphic material generated in 1982 contained the plots of calibrated radiance data points versus measurement time on thin sheets of the size 338 by 400 mm. Each individual sheet contained the radiance data taken at one wavelength and observed from two directions. Thus, for each wavelength, 3 sheets should have been generated that together contained radiation from six directions. However, it appears that for the majority of wavelengths, only one sheet was generated (or only one sheet is currently available) that included the radiances from a direction close to the zenith (1°) and a direction close to the nadir (159°), and only for a few wavelengths 3 sheets were generated representing the data from all six directions. Figure 1 shows a scan of the original sheet of the upward ($A = 5$) and downward ($A = 1$) going radiation at 0.525 μm (between the range of 0.520–0.530 μm) recorded by Venera 13. Here, the "×" and "+" marks show the printed downward radiance ($I_s\downarrow$) data points from CK1 and CK2 signal converters. Similarly, the "◇" and "□" marks show the upward radiance ($I_s\uparrow$) points. We have digitized the downward radiance data points ("×" and "+") of the first 8 wavelengths of Venera 13 in the range of 0.485–0.805 μm and they form Format 0 data products. The selection of these wavelengths is further explained in Section 3. The WebPlotDigitizer software (Marin et al., 2017) was used for the digitization process.

The radiance measurements became unrealistic while the amplification gains of the readout electronics (CK1 and CK2) were switching (Moshkin et al., 1983). An example of this phenomenon can be observed by the vertical spread of the "×" and "+'" points at ≈3400 s in Figure 1. Such outliers have been identified and removed while generating the Format 0 data products.

2.2. Format I Data Products

On the plots of original calibrated radiance data, smooth profiles were drawn (by hand) by Moshkin et al. (1983). The solid lines through "×" and "+," and "◇" and "□" marks in Figure 1 show an example of the smooth radiance profiles. N. I. Ignatiev et al. (1997) digitized these radiance profiles using the KD-5000 Digitizer and the digitized

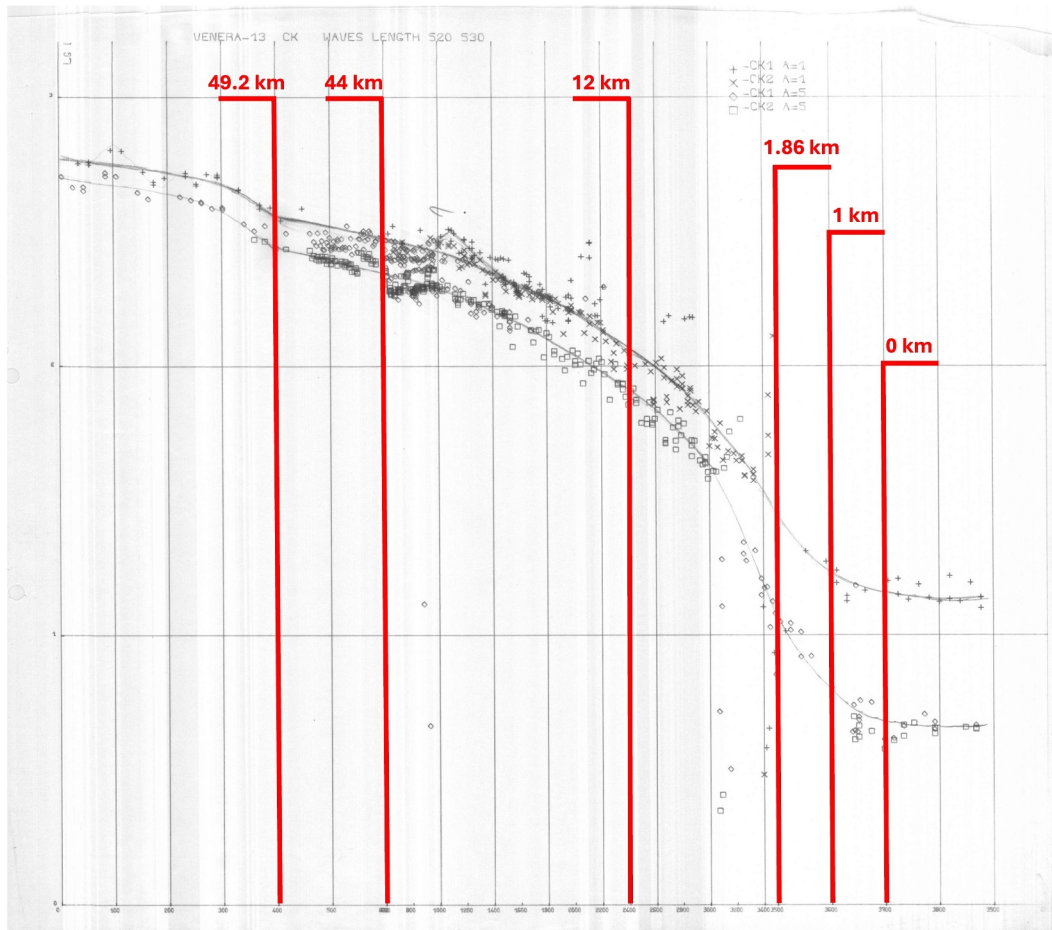

Figure 1. A scan of the original graph of calibrated radiance data (in W m^{-2} μm^{-1} sr^{-1}) versus observation time (in seconds) for Venera 13 at 525 nm (range of 520–530 nm). The "×" and "+" marks show the printed downward radiance data points from CK1 and CK2 signal converters. Similarly, the "◇" and "□" marks show the upward radiance points. The thin gray solid lines show the average radiance profiles drawn through these points. The red lines with red text are drawn over the scanned image to indicate the altitude of observation at the corresponding epoch. The red lines sequentially mark the observation times at 400, 600, 2400, 3500, 3600, and 3710 s which correspond to an altitude of 49.2, 44, 12, 1.86, 1, 0 km. The *x*-axis of the graph changes the scale at 600 and 3500 s (corresponding to 44 and 1.86 km).

radiance profiles form the Format I data set. It contains the radiance profiles of 28 wavelengths (between 0.485 and 1.145 μm) for Venera 13 and 23 wavelengths (between 0.705 and 1.145 μm) for Venera 14. Since the radiance profiles for each wavelength were separately digitized, the altitude sampling for each radiance profile was different. In general, about 55 altitude points are available for Venera 13 radiance profiles with up to 20 points below 10 km altitude. For Venera 14, about 40 altitude points are available for each wavelength with up to 10 points below 10 km altitude. The Format I Venera 13 downward radiance profiles for the first 10 wavelengths are shown in Figure 2.

2.3. Format II Data Products

Moshkin et al. (1983) introduced a few corrections (discussed in the next section) to the calibrated data and produced downward spectra and upward spectra. As seen with the Format I data, the process of generating the final calibrated and corrected spectra could have had some intermediate steps that were performed by hand. This could include carefully drawing a smooth curve (by hand) through data points of the spectra recorded at two adjacent altitudes, thus effectively averaging the spectra. However, not much information is available now about the exact nature of these processing steps. Figures 2 to 5 in Moshkin et al. (1983) provide the plots of corrected

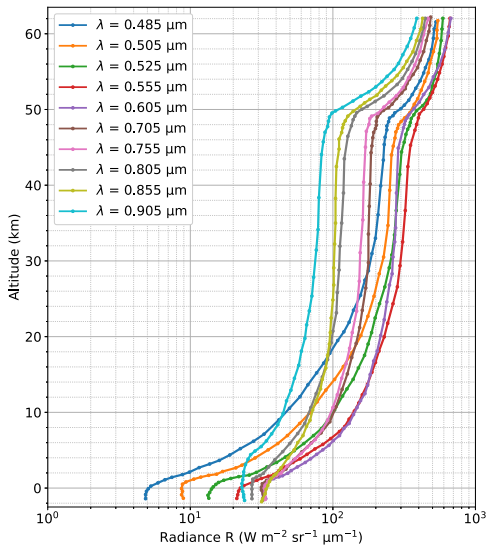

Figure 2. Venera 13 Downward radiance profiles (Format I).

data which were printed at the time of publication on large sheets that include downward spectra at 12 altitude points and upward spectra at 11 altitude points. N. I. Ignatiev et al. (1997) digitized these sheets using the KD-5000 Digitizer to form the Format II data products. While digitizing, the spectra were regularly sampled at every 0.01 μm from 0.5 to 1.17 μm for all the altitude points and the Format II data products were presented as an array of 68 wavelengths by 12 altitude points for downward and an array of 68 wavelengths by 11 altitude points for the upward spectra. As an example, the Format II Venera 13 downward spectra are shown in Figure 3.

Table 1 lists the important characteristics of all three formats. Since the figures in Moshkin et al. (1983) contain spectra only at a few altitude points, the Format II data products generated from them have much lower vertical sampling as compared to the Format I or 0 data which have the original vertical sampling of IOAV-2. Especially below 10 km, the Format II data has only 4 altitude points while the Format I or 0 data have between 20 and 40 altitude points. Thus, it is necessary to use the Format I data to check for the presence of a detached NSPL. However, the Format I data products do not include corrections applied to the Format II data. The literature describing these corrections is originally in Russian and the English translation is not widely available. For clarity, the noise estimates and the correction processes are summarized next. Also, the Format 0, I, and II reconstructed data sets have been made publicly available (N. Ignatiev & Kulkarni, 2024) as mentioned in the open research section.

2.4. Error Estimation and Correction Procedure Given by Moshkin et al. (1983)

In the original data, the behavior of the downward radiance profiles from the wide-angle spectrometer (I_w) was more monotonic and smoother than that from the scanning spectrometer ($I_s\downarrow$). For Venera 13, the discrepancy between both profiles was reported to be about 20% while that for Venera 14 was as high as 200% for higher altitudes. Moshkin et al. (1983) calculated the systematic measurement error in the original data set by considering the calibration accuracy of the spectrometer and this discrepancy between I_w and $I_s\downarrow$. This error was estimated to be ±40% for Venera 14. Due to unknown reasons, the systematic measurement error was not estimated for Venera 13. However, it is expected to be much smaller than that of Venera 14. This is because the discrepancy between I_w and $I_s\downarrow$ was much smaller for Venera 13 than 14. Moshkin et al. (1983) also estimated the random error in the original scanning spectrometer data set (I_s) by taking a standard deviation of the radiance data points as compared with the smoothly drawn curve. This error was found to be 10–15% for Venera 13 and 5–7% for Venera 14.

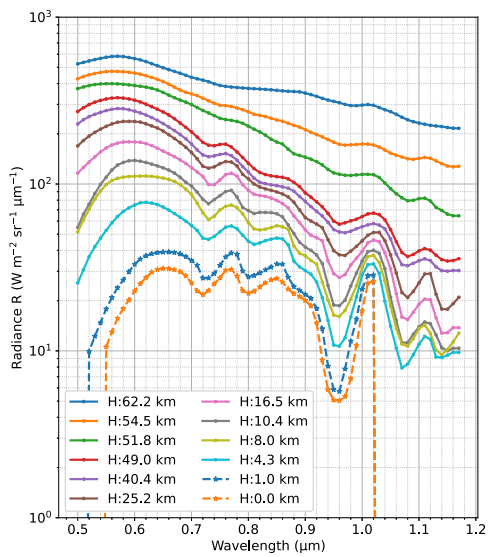

Figure 3. Venera 13 Downward Spectra (Format II). The image is reproduced from Moshkin et al. (1983).

Since I_w profiles were more monotonic and smoother than $I_s\downarrow$ profiles, Moshkin et al. (1983) considered the I_w profiles to be more reliable. But for both probes, $I_w < I_s\downarrow$. Thus, I_w was increased by a constant multiplying factor $\left(\sqrt{\frac{I_s\downarrow}{I_w}}\right)$ which was calculated to be 1.07 and 1.5 for Venera 13 and 14 respectively. Then, $I_s\downarrow$ was corrected such that it coincided with the smooth I_w profiles. Also, the wide-angle spectrometer did not record the upward radiation, hence this correction was not possible for $I_s\uparrow$ profiles.

For altitudes below 7 km, the thermal radiation due to heated parts of the instrument became detectable. This radiation was found to be significantly less as compared to downward radiation. The parts of the spectra that have been significantly affected have been cut off and can be seen as vertical lines in Figure 3. However, this thermal radiation was considerable as compared to upward radiation. Hence, Moshkin et al. (1983) calculated the values of $I_s\uparrow$ at the surface by combining $I_s\downarrow$ at the surface and ground albedo values from Venera 9 and 10 landing sites given by Y. M. Golovin (1979).

Table 1
Brief Description of the Three Formats of the Reconstructed Venera 13 Spectrophotometric Data

Name	Format 0	Format I	Format II
Digitization Source	Plots of calibrated radiance profiles on sheets of the size 338 by 400 mm	The same as Format 0, first provided by N. I. Ignatiev et al. (1997)	Plots of calibrated and corrected spectra printed on nearly A3 size sheets for Moshkin et al. (1983)
Type of Data	Printed radiance data points	Smooth curves drawn through printed radiance data points	Printed spectra at multiple altitude levels
Description	Downward radiance profiles	Downward and upward radiance profiles	Downward and upward spectra at 12 and 11 altitude levels, respectively
Wavelength Range	0.485 to 0.805 μm	0.485 to 1.145 μm	0.5 to 1.17 μm
Type of spectral sampling	Irregular	Irregular	Regular (at 0.01 μm)
Number of spectral points	8	28	68
Type of altitude sampling	Irregular, as per original measurements	Irregular	Irregular
Number of altitude points	Varying, 150 to 260 points	Varying, 30 to 55 points	12 downward spectra, 11 upward spectra

3. Error Estimation and Correction Procedure for the Format I Data

As discussed before, the Format II data contains the corrections designed by Moshkin et al. (1983). However, due to the loss of the original data set, we do not have all the required radiance profiles from I_w to recreate the correction processes and apply them to the Format I $I_s\downarrow$ data. It also appears that the $I_s\uparrow$ was corrected but these corrections are not specifically mentioned in the Moshkin et al. (1983). Unfortunately, the authors of the data set have passed away and at which step of the data processing after the calibration, the calibrated radiance plots were generated (that were used to generate Format 0 and Format I data) is not fully clear. Thus, before using the Format I data for retrievals, we compare it with the Format II data, to check the degree of difference between the non-corrected and the corrected data. Based on this, the most useful and unaffected part of the Format I data is identified which is later used for the retrievals. We also correct small discrepancies observed in the Format I data and identify the effects of the digitization process on the data set. This is described in more detail in the next subsections.

3.1. Comparison of Format I and II Data Sets

Both Formats are compared by selecting the data from a common grid of altitude versus wavelength. For example, a common grid of 28 wavelengths by 11 altitudes is selected for the Venera 13 downward data and is shown in Figure 4a. Here, the solid lines indicate the Format I data and the dashed lines indicate the Format II data. Then selected data from Format II was divided by Format I data. As shown in Figure 4b, a mismatch going from +20% to −20% can be noticed (shortward of 0.9 μm). A similar procedure was followed for the Venera 13 upward, Venera 14 downward and upward data.

To assess the mismatch between both Formats, a mean and standard deviation of the absolute mismatch (in %) are provided in Table 2. These values provide a combined quantification of (a) the correction processes performed by Moshkin et al. (1983) and (b) the errors that might have been introduced while digitizing both data sets. It can be observed that both the downward and upward Venera 14 data sets show a higher mismatch than that of Venera 13. However, a few more of the original graphs of Venera 14 data have been found that contain wavelengths less than 0.705 μm. The digitization of these graphs to reconstruct corresponding Format 0 and I data products is currently underway which is being dealt with as a separate study while this paper focuses only on the Venera 13 data.

Next, the values of mismatch are higher for upward data sets than for downward data sets. From this, it is evident that some other correction must have been employed to plots used for the Format II Upward data sets, however, this correction is not described in Moshkin et al. (1983). Thus, out of Venera 13 downward and upward data sets, we find that the Venera 13 Format I Downward data is more consistent with the Format II (corrected) data. Since

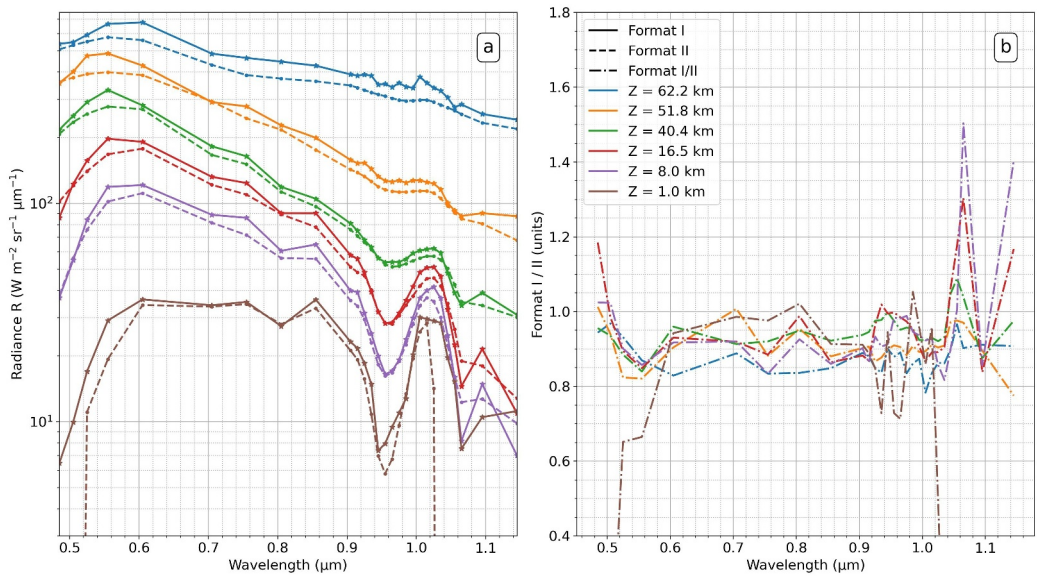

Figure 4. (a) Venera 13 Downward Radiances from Format I (solid lines) and Format II (dashed lines) interpolated on a common grid of 28 wavelengths by 12 altitudes. Out of 12, only 6 altitudes are shown for clarity. (b) Corresponding Comparison of Format I and Format II spectra (dash-dotted lines).

the Upward data was affected by thermal noise in the lowest 7 km, we have used only the Downward data for the final retrievals.

3.2. Wavelength Offset in Format I

Although the Format I spectra have fairly low wavelength sampling, prominent features such as the strong absorption band of H_2O at 0.95 μm and surface thermal emission at 1 μm can be well distinguished in Figure 4a. Careful observation reveals that the Format I spectra seem to have a small offset with respect to the true positions of the prominent features when compared with the simulations. Thus, the Venera 13 and 14 Format I Downward data sets were corrected for a wavelength offset of −0.0150 μm and +0.0025 μm, respectively. These corrections are applied to the spectra before using them for retrievals.

3.3. Distorted H_2O Absorption Band and Surface Thermal Emission Feature in Format I

Even after correcting for the wavelength offset, the surface thermal emission features at 1 and 1.1 μm appear to be quite distorted and Figure 4b shows a highly fluctuating mismatch up to +40%. Also, the shape of 0.95 μm H_2O absorption band appears to be distorted for all Format I data sets at altitudes above 40 km and below 8 km. For example, the spectra at altitudes of 62.2 and 1 km in Figure 4a. The Format II data has been previously used by N. I. Ignatiev et al. (1997) to retrieve water vapor content in the atmosphere. While some parts of the Format I data set (between 40 and 8 km) could also be used to retrieve water vapor content in the deep atmosphere, this is not the goal of the current study. Hence, considering the above distortion in the data set, it was decided to cut off the Format I spectra at 0.9 μm. The reason for this distortion is currently not known.

Table 2
The Mean and Standard Deviation for the % Mismatch Between Format I and II of Secondary Data Sets

Data sets	Mean (%)	Standard deviation (%)
Venera 13 Downward	11.51	9.16
Venera 13 Upward	15.78	17.47
Venera 14 Downward	20.50	13.31
Venera 14 Upward	26.49	18.80

3.4. Excessive Smoothing of the Radiance Profiles at ≈1 km Altitude

Figure 5 shows a zoomed-in version of the Format I Venera 13 Downward radiance profile for altitudes below 30 km for all wavelengths below 0.9 μm. It can be observed that the radiance profiles for most wavelengths change slope and become nearly vertical from about 1 km altitude down to the surface. In other words, the radiance remains nearly constant below the altitude of 1 km. However, as per the radiative transfer simulations (discussed in the next section), the expected radiance should continue to decrease down to the surface instead of remaining constant from 1 km down to the surface. In our

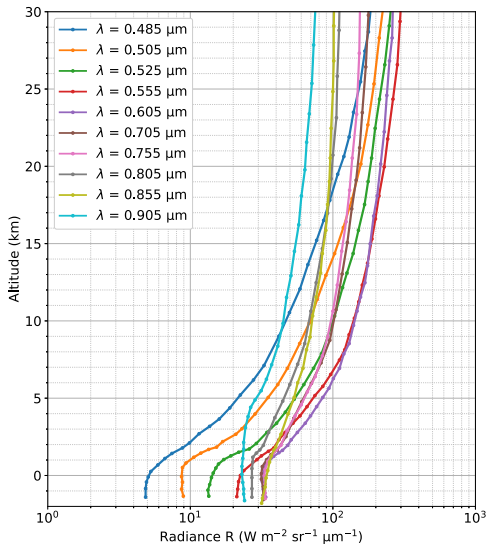

Figure 5. Format I Venera 13 Downward radiance profile for 10 wavelengths from 0.485 to 0.905 μm without using interpolation.

simulations adding a localized change in the surface albedo or surface temperatures, or increasing the VMR of prominent absorbing gases like CO_2 and H_2O cannot replicate the change in the slope of radiance profiles at 1 km. Figure 1 shows the smooth profile hand-drawn between the data points. Here, the excessive smoothing between the 3300 and 3700 s seems to be responsible for the change of slope observed at 1 km (≈3600 s).

As an exception to this anomalous behavior, the radiance profile of $\lambda = 0.905$ μm (cyan profile in Figure 5) becomes nearly vertical at a higher altitude of ≈4.5 km and the radiance profile of $\lambda = 0.855$ μm (yellow line) does not show any change at all. On the original graphs, these two radiance profiles seem to have fewer radiance data points than the other 8 radiance profiles. Thus, they seem to have been affected by a different cause than that which is causing the change of slope at 1 km. Hence, these wavelengths are not considered in our analysis which further reduces the number of available radiance profiles to 8.

3.5. Change of Scale of the x-Axis on Original Graphs

Looking closely at Figure 1 another discrepancy can be observed. At 3500 s (equivalent to 1.86 km), the graph changes the scale of the *x*-axis from 1 division = 400 s to 1 division = 100 s. When the radiance profiles drawn on the original graphs are transferred onto a graph with a uniform scale for the *x*-axis, the radiance profiles show a sudden change of slope at the point where the scale is changed. Thus, the change of slope of the radiance profiles at ≈1 km could have been a combined effect of excessive smoothing as discussed above and the change of the scale at 3500 s (1.86 km).

3.6. Data Preparation for the Near-Surface Retrievals

In this way, out of the Venera 13 and 14, upward and downward Format I data, we select the first eight Venera 13 downward radiance profiles as the best candidates for the retrievals. However, even these profiles are affected by (a) the change of slope at ≈1 km and (b) the change of scale at 3500 s (1.86 km). To find out the degree to which these phenomena affect the retrievals we use the following four cases of radiance profiles for the retrievals:

1. Format I radiance profiles till the surface (=3710 s)
2. Format I radiance profiles till 1.86 km altitude (=3500 s)
3. Format 0 binned radiance profile (bin size = 0.5 km)
4. Format 0 binned radiance profile (bin size = 1 km)

Comparing the results of Cases 1, 2, and 3 we can find out the effects of change of slope at ≈1 km and change of scale at 3500 s (1.86 km) on the retrievals. The Format 0 data is also considered since it is free from the effect of change of slope at 3500 s and does not have any smoothing applied causing a change of slope at 1 km.

However, the radiance data points of Format 0 data cannot be directly used as the input for our retrievals. To use the Format 0 radiance points as the input for retrievals, the radiance points are binned into altitude bins of 0.5 km. Within a single bin, all the collected data points are averaged and the average value is assigned at the center altitude of the bin to create the radiance profiles. To ensure that the binning process described above does not introduce unwanted effects, the results of Case 3 are compared with Case 4 which has larger bins of size 1 km. Figure 6 shows the plot of Format 0 radiance points and binned radiance profiles (with a bin size of 0.5 and 1 km) for two wavelengths (0.485 and 0.605 μm).

Considering the random error in the original data, and the mismatch between the Format I and Format II data sets, a conservative estimate of 10% measurement error is used on the radiance profiles from all four Cases. For Cases 3 and 4, there are some bins without any radiance data. Such bins are filled with linearly interpolated values, and a measurement error of 100% is set for them. This ensures that the radiative transfer and retrieval tool (discussed in Section 4) only fits the points where original radiance data exists and not the bins where an interpolated value is placed.

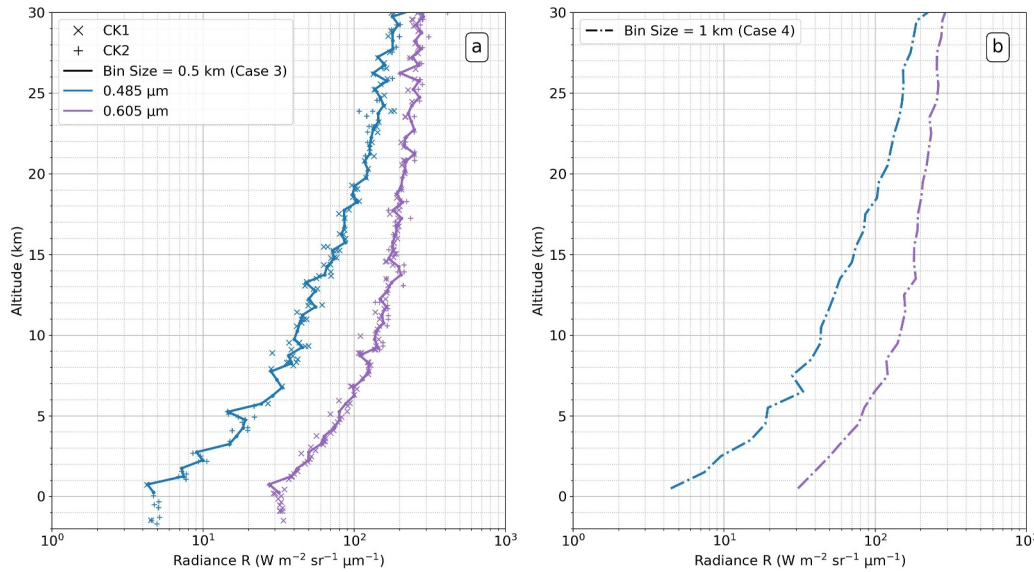

Figure 6. (a) The plot of Format 0 Calibrated Radiance data points versus altitude. The time values from the original graphs have been converted to the corresponding altitude values. The "×" and "+" marks show the downward radiance data points on the original graphs from CK1 and CK2 signal converters (Figure 1 shows an example of the original graphs). Different colors indicate different wavelengths. The solid lines indicate the binned profile with altitude bins of 0.5 km (Case 3). (b) The dash-dotted lines indicate the binned profile with altitude bins of 1 km (Case 3).

4. Radiative Transfer: Methods and Assumptions

NEMESIS, a radiative transfer and retrieval tool (P. G. J. Irwin et al., 2008), is used in this work to interpret the Venera 13 spectra. NEMESIS contains a forward model and a retrieval algorithm that work simultaneously. For the forward model, the multiple-scattering in a plane-parallel atmosphere is computed using the matrix-operator scheme given by Plass et al. (1973). P. Irwin et al. (2020) modified the multiple scattering model to extract the spectrum at the given altitudes inside the atmosphere that can be used to fit in situ observations. Thus, for retrievals, the in situ spectra recorded (a) in the downward and upward direction or (b) in the downward direction at various altitudes within the atmosphere are given as input. Then NEMESIS simultaneously fits the spectra at all given altitudes to produce the required retrievals. These retrievals are performed using a modified optimal estimation technique (P. G. J. Irwin et al., 2008; Rodgers, 2000).

To generate an accurate forward model, various parameters are required that focus on different aspects of the atmosphere of Venus. The model atmosphere is constructed by using the pressure, temperature, gravity, and density profiles for latitudes up to 30° from the Venus International Reference Atmosphere (VIRA) (Seiff et al., 1985). The molecular Rayleigh scattering is considered for CO_2, and N_2, while molecular absorption is considered for CO_2, H_2O, CO, HCl, HF, H_2S, OCS, SO_2. The volume mixing ratio of H_2O, CO, HCl, HF are taken from Bézard et al. (1990) and those of H_2S, OCS, SO_2 are taken from Hunten et al. (1983). Figure 8a shows the profiles of volume mixing ratios for the minor species. The volume mixing ratio of CO_2 and N_2 are constant and are equal to 0.965 and 0.035 respectively (Marcq et al., 2018).

4.1. Spectral Data for the Absorbing Species

The dominant absorbing species in the Venusian atmosphere are CO_2 and H_2O. The absorption cross-sections for these gases are usually calculated using the High-Temperature Molecular Database (HITEMP). While developing the HITEMP 2010 database (Rothman et al., 2010), the HITEMP 1995 CO_2 database (Rothman et al., 1995) was replaced by a more accurate CDSD-1000 database (Perevalov & Tashkun, 2008). However, this database (Rothman et al., 2010) has gaps in the wavelength intervals around 0.85, 0.95, and 1.15 μm. This can be observed from Figure 7 shown by the solid blue line. Pollack et al. (1993) computed a high-temperature CO_2 database specifically for Venus which provides missing spectral lines to accurately model the 1 and 1.7 μm windows (solid green line). This database is referred to as the HITEMP-Venus database but does not cover the region between 0.8

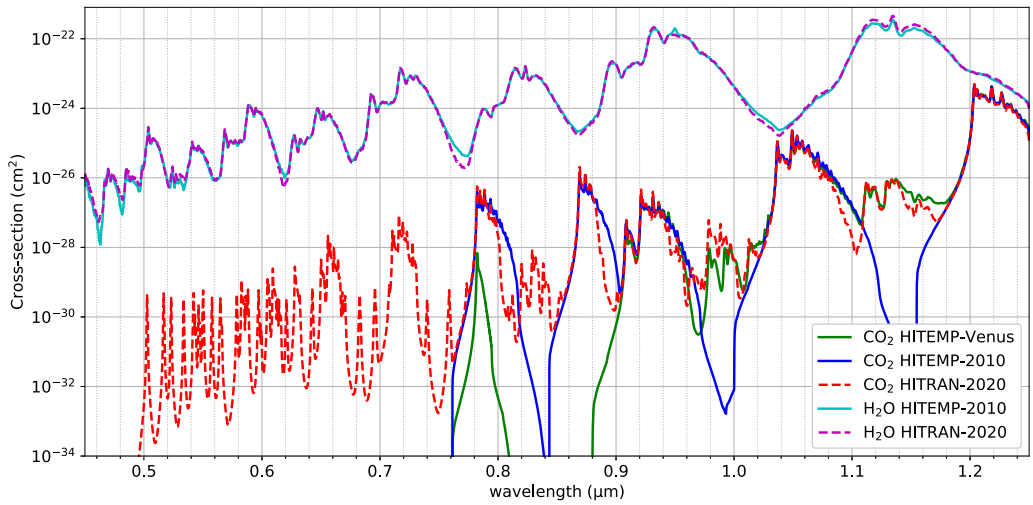

Figure 7. Comparison of the CO_2 and H_2O absorption cross-sections using different databases at a pressure of 20 atm and temperature of 575 k.

and 0.9 μm. The High-Resolution Transmission molecular absorption database (HITRAN) was recently updated (Gordon et al., 2022) and now includes a number of lines that cover the intervals discussed above (dashed red line). Hence, we calculate the absorption cross-section of CO_2 using the HITRAN 2020 database.

The spectral parameters of H_2O are taken from the HITEMP2010 database for consistency with previous studies. However, as shown in Figure 7 there is a good match between the HITEMP2010 (cyan) and the HITRAN2020 (magenta) H_2O line data. CO and SO_2 also show small absorption in the wavelength range of Venera 13 and 14 observations. Apart from these, absorption from four minor absorbing species—OCS, HCl, HF, H_2S is also considered in the model atmosphere. The spectral parameters of CO, HCl, HF, H_2S, OCS, and SO_2 are taken from HITRAN 2020 (Gordon et al., 2022).

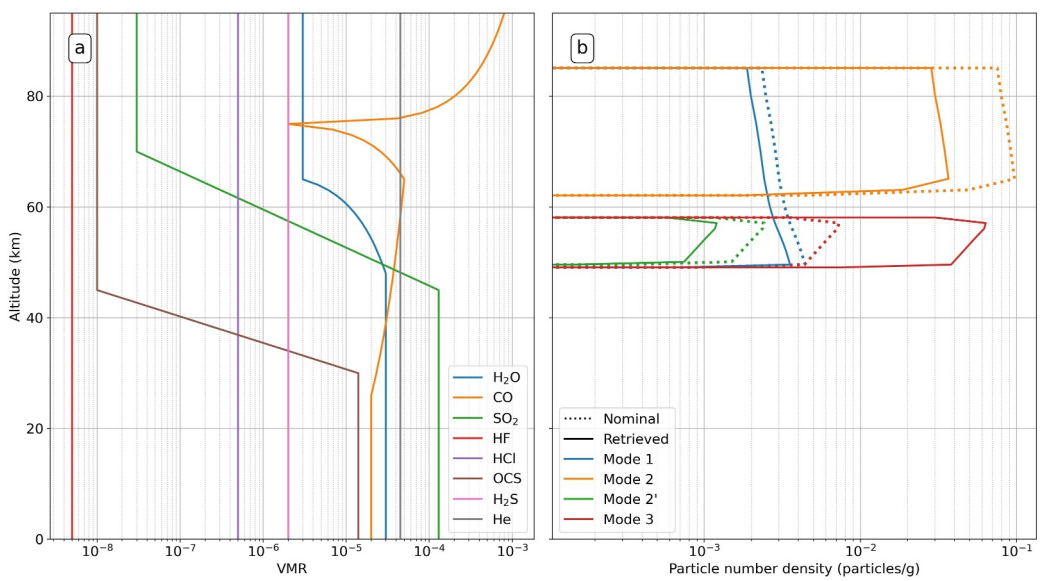

Figure 8. (a) Vertical profile of the volume mixing ratios of the gaseous species considered in the model atmosphere. (b) Nominal cloud particle number density profiles (dashed lines) from Barstow et al. (2012) and cloud particle number density profiles retrieved from Venera 13 data (solid lines).

4.2. Line Shape Calculations

Due to the extreme conditions in the atmosphere of Venus, the effects of thermal Doppler and pressure broadening on the absorption line shapes become important. A Gaussian profile best describes the Doppler broadening while the pressure broadening is best described by a Lorentzian profile (Goody & Yung, 1989). Hence, it is a standard practice to use the Voigt profile, which is the convolution of both of these profiles, to describe the line shapes (Pollack et al., 1993). Thus, for all the species except CO_2, a full Voigt profile is calculated with a line cutoff at 120 cm^{-1}.

In the deep atmosphere, the pressure broadening dominates for CO_2 and the Voigt profile reduces to a Lorentzian profile. However, due to high pressure, the effect of collisional line mixing also becomes important, in which the optical thickness far from the line center decreases more rapidly than that predicted by the Lorentzian profile, causing a narrowing of the line. Because of the collisional line mixing, the lineshapes of CO_2 are best described by sub-Lorentzian line profiles (Burch et al., 1969). This profile is commonly modeled as a product of the Lorentz profile and a correction factor (χ). Following the approach of Tsang et al. (2008), we calculate the sub-Lorentzian line profile for CO_2 with a correction factor (χ) given by Tonkov et al. (1996) along with a line cutoff at 120 cm^{-1}.

Given that CO_2 is the abundant gas, the broadening of half widths by CO_2 is also important for the Venusian atmosphere. While calculating the lineshape of CO_2 the CO_2-CO_2 self-broadening half widths are used. For H_2O lineshape calculations, CO_2–H_2O foreign-broadening is considered by multiplying the air-broadened half widths, taken from HITEMP2010, by a constant factor of 1.3 (Howard et al., 1956; Pollack et al., 1993). The effect of the remaining species on the low-resolution spectra is much less as compared to CO_2 and H_2O. Thus, for simplicity, they have been simply air-broadened using the air-broadening half-widths from the above-mentioned databases.

The collision-induced absorption (CIA) of CO_2 is another source of opacity for the Venusian atmosphere. The contribution due to CIA is difficult to determine experimentally and it is usually modeled with the help of a CIA coefficient (α) which is the function of the square of atmospheric density (Snels et al., 2014). It plays a significant role in the nightside thermal emission modeling within the near-IR windows (Pollack et al., 1993). Previously, α has been determined to be $5.38 \cdot 10^{-3}$ cm^{-1} $amagat^{-2}$ for the wavelength range of 6.66–8.33 μm (Manzanares et al., 1984), $1.6 \cdot 10^{-6}$ to $2 \cdot 10^{-7}$ cm^{-1} $amagat^{-2}$ for 2.3 μm window (Tonkov et al., 1996), and $5 \cdot 10^{-9}$ cm^{-1} $amagat^{-2}$ for 1.74 μm window (de Bergh et al., 1995). Following this decrease in value of α as we move towards shorter wavelengths, Mueller et al. (2020) derive a value of $1.9 \cdot 10^{-10}$ cm^{-1} $amagat^{-2}$, while Arney et al. (2014) determine a value of 0 cm^{-1} $amagat^{-2}$, that is, no CIA for the 1.02 μm window. Thus, shortward of 1 μm it is safe to assume that the contribution due to the CIA is not significant and this source of opacity is not included in our simulations.

4.3. Rayleigh Scattering

Various parameterizations have been previously used to model the Rayleigh scattering in Venus' atmosphere. The variability originates from (a) variations in the approximation, (b) consideration of dominant species (pure CO_2 vs. a mixture of 96.5% CO_2 and 3.5% N_2, (c) the properties of dominant species (refractive index and depolarization coefficient). The Rayleigh scattering column optical thickness, $\tau_{msca} \propto \lambda^{-4}$. Showing a rather opposite behavior to that of CIA, Rayleigh scattering does not contribute significantly to the nightside thermal emission simulations in the near-IR range but is an important parameter for simulations in the visible range. We have tested a few different parameterizations from previous authors as explained next. Model A follows the approach of Bézard et al. (2009) that uses a simple approximation considering a pure CO_2 composition given in Equation 1.

$$\tau_{msca} = \frac{8.8 \times 10^{-28}}{\lambda^4} \times \rho_n \tag{1}$$

Here, the wavelength, λ, is in μm and the particle number density, ρ_n, is in particles per cm^2. Next, Equation 2 shows Model B that follows the approach used by N. I. Ignatiev et al. (1997) considering both CO_2 and N_2 gasses in the atmosphere.

Table 3
The Rayleigh Scattering Column Optical Thickness τ_{msca} at 0.63 μm and 1.00 μm for Different Rayleigh Scattering Models

Rayleigh scattering model	τ_{msca} at 0.63 μm	τ_{msca} at 1.00 μm
A: Bézard et al. (2009) (CO_2)	8.3323	1.3126
B: Ignatiev et al. (1997) (CO_2 and N_2)	9.6538	1.4913
C: Ignatiev et al. (1997) (CO_2 and N_2 gradient below 7 km)	9.6829	1.4958
D: Ignatiev et al. (1997) (CO_2)	9.8549	1.5223
E: Hansen and Travis (1974) (CO_2)	9.6912	1.4975

$$\tau_{msca} = \frac{\kappa_B}{10\lambda^4} \times \left(\frac{17.904\nu_1}{\left(156.63 - 1/\lambda^2\right)^2} + \frac{11.041\nu_2}{\left(189.94 - 1/\lambda^2\right)^2} \right) \times \rho_n \tag{2}$$

Here, κ_B is the Boltzmann constant, ν_1 and ν_2 denote the volume mixing ratios of CO_2 and N_2 respectively, while λ and ρ_n follow the previous units. Model C follows the same formulation as Model B, but includes a composition gradient below 7 km altitude as proposed by Lebonnois and Schubert (2017). In this model, the volume mixing ratio of N_2 decreases linearly with the logarithm of pressure from 0.035 at 7 km to 0 at the surface. The volume mixing ratio of CO_2 correspondingly increases from 0.965 at 7 km to 1 at the surface. Along with Rayleigh scattering, this composition gradient is also applied while calculating the absorption cross-sections of CO_2. Next, Model D uses the same formulation as Model B but now uses a pure CO_2 atmosphere. Lastly, another simplified formulation of Rayleigh scattering for pure CO_2 atmosphere of Venus given by Hansen and Travis (1974) is shown by Equation 3.

$$\tau_{msca} = 1.483\lambda^{-4}\left(1 + 0.013\lambda^{-2}\right) \tag{3}$$

Here, the λ follows previous units and the equation is adjusted for a mean planetary radius of 6,052 km.

Table 3 shows the calculated values of τ_{msca} for all the above models at 0.63 μm and 1.00 μm. As discussed above, the value of τ_{msca} is much higher at 0.63 μm as compared to at 1.00 μm. While considering a pure CO_2 atmosphere, Model A gives a conservative estimate of τ_{msca}, while Model D provides a higher estimate, closely followed by Model E. Comparing Model B and D, it can be observed that a mixture of 96.5% CO_2 and 3.5% N_2 shows a slightly lower value of τ_{msca} than that of pure CO_2. This is expected considering at 1 atm pressure level pure CO_2 shows ≈70% more τ_{msca} than pure N_2 (Hansen & Travis, 1974). Thus, Models A and B are considered for further simulations, with Model A representing the lower end and Model B representing the higher end of τ_{msca} values. Since the difference in the values of τ_{msca} from Models D and E is not significant, also Model D uses the same formulation as Model B except for the atmospheric composition, Models D and E are not considered further. Model C investigates the effect of a composition gradient (Lebonnois & Schubert, 2017) below 7 km. Since the gradient slightly increases the volume mixing ratio of CO_2 in the atmosphere, the value of τ_{msca} also shows a slight increase when compared to Model B. Although the magnitude of this increase is small, the extra optical thickness is added below 7 km which is in the altitude range of the near-surface particulate layer (NSPL) being investigated in this work. Thus, Model C is also considered in further simulations.

4.4. Clouds and Hazes

A cloud model adapted to VIRTIS/Venus Express observations by Barstow et al. (2012) is used to model the Main Cloud Deck (MCD). It is based on the cloud model initially developed by Crisp (1986) using Pioneer Venus data and later modified by Pollack et al. (1993) using data from the Galileo/NIMS Venus flyby. The model contains four cloud modes whose size distributions follow a log-normal parameterization defined in Equation 4 (Thomas, 1987).

$$n(r) \propto \frac{1}{r} \exp \frac{-(\ln r - \ln R)^2}{2\sigma^2} \tag{4}$$

Table 4
Geometric Mean Radius (R) and Geometric Standard Deviation (σ) of Cloud Modes

Mode	R	σ
1	0.30	0.44
2	1.00	0.25
2'	1.40	0.21
3	3.65	0.25

Here, R is the geometric mean radius and σ is the geometric standard deviation. The values of R and σ for the four particle modes are listed in Table 4 and the nominal particle number densities are shown by dotted lines in Figure 8b. In this cloud model, the variations in the cloud optical thicknesses can be easily simulated by multiplying the number densities of various modes by different scaling factors.

Mode 2 particles are considered to be composed of concentrated sulfuric acid (85% H_2SO_4) particles which are produced photo-chemically (James et al., 1997; Taylor, 2006) while the composition of Mode 1 and 3 is not yet known (Limaye et al., 2018). Thus, the usual assumption that all the four modes have the same composition, viz., 85% H_2SO_4 (Haus & Arnold, 2010; Pollack et al., 1993; Tsang et al., 2008) is followed to model the clouds. The refractive indices for this composition are taken from Palmer and Williams (1975). The upper cloud deck of Venus also shows the presence of a mysterious UV absorber, which helps to trace the dynamic behavior of clouds. The UV absorber causes additional absorption, but its chemical origin or composition is not yet known. This phenomenon can be modeled by modifying the single scattering albedo (ϖ) of Mode 1 particles as shown by Crisp (1986) which is further explained in Section 4.5. Lastly, the particles in the NSPL are named Mode 4 Particles following a similar nomenclature as that of MCD. The properties of the Mode 4 particles are unknown; the extent to which their refractive index and size distribution can be constrained is discussed later in Section 5.3.

4.5. Updating the Atmospheric Model to Match the Local Cloud Conditions

The MCD shows continuous localized variations and thus, the nominal properties of the above-discussed cloud model need to be updated with their local values at the time of in situ measurements. These include (a) the cloud base altitude, (b) the abundances of four MCD modes (1,2,2′,3), and (c) absorption from the unknown UV absorber (imaginary refractive index of Mode 1 particles). To estimate these parameters, retrievals are set up using the setup described in the previous subsections. For scattering calculations in NEMESIS, the number of layers in the model atmosphere is limited to 39. So, a customized layering scheme is used to discretize the model atmosphere with a finer altitude grid in MCD ($\Delta H = 0.5$–1 km) and a coarser altitude grid elsewhere ($\Delta H = 5$–10 km). This scheme is termed "Layering scheme 1" and the base altitudes of this scheme are listed in section Appendix A. The Venera 13 Format-I downward radiance profiles with an estimated error of 10% are used as the input for NEMESIS. A total of 26 radiance profiles from 0.47 to 1.05 μm are used. The input is given in the form of spectra interpolated at 21 base altitude points between 30 and 58 km from the Layering scheme 1.

To retrieve the base altitude of MCD, 11 retrievals are performed by changing the base cloud altitude in the nominal model from 46 km up to 51 km in steps of 0.5 km. At the same time, NEMESIS is set up to retrieve the scaling factors on the nominal number densities of all four cloud particle modes. An a priori scaling factor of 1.0 is used for all four modes with 100% error, which means that NEMESIS is essentially free to retrieve the scaling factor for an optimal fit.

To account for the absorption from the UV absorber, the modified single scattering albedo (ϖ) of Mode 1 particles given by Crisp (1986) is first used, but the fits with the Format I radiance profile were bad especially shortward of 0.6 μm. Hence, it was decided to retrieve the ϖ using NEMESIS to improve the fits. In NEMESIS, the single scattering albedo is indirectly retrieved by performing imaginary refractive index (η_i) retrievals. As per Crisp (1986), the magnitude of absorption due to the unknown UV absorber decreases with an increase in wavelength and is negligible longward of 0.8 μm (brown line in Figure 9). Also, η_i retrievals could mask absorption by other species. So it was necessary to put a priori constraints on η_i such that the absorption mimics the decreases with increasing wavelength. Based on this, instead of using a constant a priori value for η_i for the entire wavelength range, it was smoothly varied from 10^{-3} at 0.48 μm to 10^{-6} at 1.1 μm with an error of 100%. This forces the η_i retrievals to simulate the absorption of the UV absorber at short wavelengths, but tend smoothly to conservative scattering at longer wavelengths while fitting the radiance data. Meanwhile, the real part of the refractive index (η_r) of Mode 1 particles was chosen to be 1.43698 at 0.63 μm based on the 85% H_2SO_4 composition Palmer and Williams (1975) and the Kramers-Kronig relation is used to reconstruct the real part of the complete refractive index spectrum.

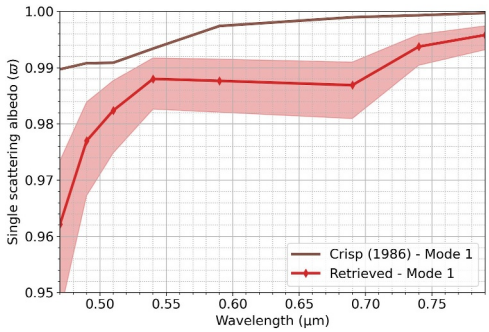

Figure 9. Single scattering albedo of Mode 1 particle retrieved from Venera 13 data (red line) in comparison with that given by Crisp (1986) (brown line).

From the 11 retrievals with different base altitudes, the best χ^2/n fit (0.89) is achieved for a base altitude of ≈49 km and the resulting particle number density profiles are shown in Figure 8b by the solid lines. The retrieved base altitude is consistent with the lower cloud boundary determined by the Venera 13 Nephelometer (Marov et al., 1983). The nephelometer readings also show a reduced volume scattering coefficient from 59 km up to 62 km which is again consistent with the retrieved cloud number densities that have only Mode 1 present in that altitude range. This also serves as a validation for our radiative transfer model. The above retrievals are performed while using the Rayleigh scattering Model A. The retrievals using Models B and C retrieve similar cloud particle number density profiles and ϖ values. Thus, they are not separately discussed in this step. This behavior is expected since atmospheric density is much lower in the altitude range of clouds as compared to the deep atmosphere and the effects of different Rayleigh scattering models will become more prominent in the deep atmosphere.

The retrieval using the ϖ given by Crisp (1986) (instead of retrieving ϖ) with the same cloud base altitude (49 km) and retrieving the scaling factors for four modes of MCD results in slightly worse fits ($\chi^2/n = 1.21$) when compared with the retrievals discussed above. In Figure 9,the ϖ given by Crisp (1986) (brown line) is compared with the retrieved ϖ (red line). Our retrievals show a higher absorption overall and a much higher absorption shortward of 0.54 μm. While η_i retrievals could mask absorption from other species, the known absorbing species in the atmosphere do not show all of these features either independently or in combination with other species. Thus, these features may be unique to the unknown UV absorber. However, more tuning is required to draw conclusions about the absorption due to the unknown UV absorber and this will be dealt with in a separate manuscript. Considering we have achieved reasonably good spectral fits for the current study ($\chi^2/n < 1$), we update the model atmosphere with the retrieved properties of MCD (i.e., the abundances of Modes 1 to 3 and refractive index of Mode 1 particles), and shift our focus to the near-surface retrievals.

5. Near-Surface Retrievals

After adapting the upper and middle atmosphere in the model to the local conditions at the time of the Venera 13 landing, we are now ready to perform near-surface retrievals. Due to the limit of 39 atmospheric layers in NEMESIS, the model atmosphere is now discretized using the Layering Scheme 2 (section Appendix A). This scheme has a high vertical resolution in the deep atmosphere ($\Delta H = 0.5$ km) and a low vertical resolution elsewhere ($\Delta H = 5$–10 km). The radiance profiles below 30 km are used. As explained in Section 3.6, 8 radiance profiles (0.47–0.79 μm) are used for the near-surface retrievals. Various retrievals performed using this setup are described next.

5.1. Test Runs Without an Added Extinction Source

First, we examine the hypothesis that the NSPL did not exist at the time of the Venera 13 landing by performing three test runs. These runs use the Case 3 radiance profiles from Section 3.6 (the Format 0 binned radiance profiles with a bin size of 0.5 km) recorded below 30 km. Figure 10 shows the Case 3 radiance profile for two wavelengths (0.47 and 0.59 μm) by the dotted lines and assumed error on the profiles by the shaded region.

In Run A, a forward simulation is carried out using the updated atmospheric model. The simulated radiance profiles from this run are shown by the dash-dotted line in Figure 10. To check the agreement between the measured (Case 3) and simulated radiance profiles a χ^2/n value is calculated. It can be observed that the correspondence between the simulated and measured radiance profiles is not that good with χ^2/n = 74.5.

Run B uses the same atmospheric model, but now NEMESIS re-retrieves the abundance of cloud Modes 1 to 3 in MCD while fitting the Case 3 profiles below 30 km. This leads to a greater optical depth in the MCD, in order to obtain a better match for the lower atmosphere radiance levels. Therefore, Run B achieves better fits than Run A (χ^2/n = 6.37). However, without particulates in the lower atmosphere, the vertical gradient of the calculated radiance is not as large as that observed. Run B exhibits a χ^2/n > 1 which shows that the fitted radiance profiles are

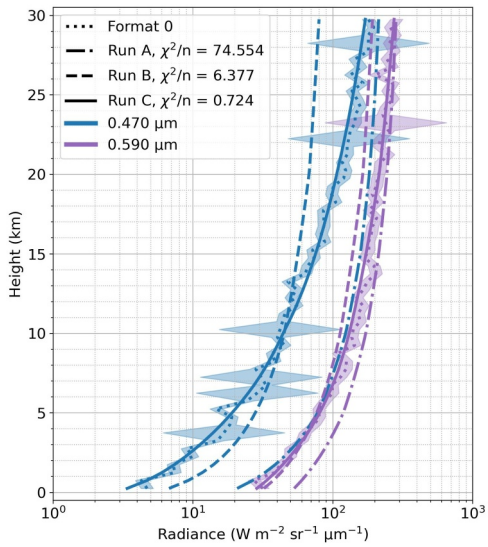

Figure 10. Case 3 radiance profiles (dotted) and fitted radiance profiles (dash-dotted, dashed and solid lines) from three runs. Run A and B represent the null hypothesis (no particulates below the main cloud deck), with different assumptions about main cloud deck parameters (Section 5.1). Run C shows the radiance profiles once a near-surface particulate layer is retrieved (Section 5.2). Different colors indicate different wavelengths. See the text for an explanation.

not within the measurement error on the Format 0 radiance profiles. Therefore, we conclude that an additional source of extinction in the deep atmosphere is needed.

More extinction can be added by a uniformly dispersed haze or by a detached particulate layer. This is achieved by introducing the "Mode 4" particles into the model atmosphere and allowing NEMESIS to retrieve their properties while fitting the radiance profiles. This is discussed next.

5.2. Detection and Retrieval of Mode 4 Abundance Profile

As explained in Section 1, limited information is available about the size, shape, abundance, refractive index or composition of mode 4 particles that could form the hypothesized NSPL. As a first approximation, we assume a spherical shape for Mode 4 particles while performing the Mie scattering calculations. After this, the unknowns for retrievals include the particle size distribution, abundance, and refractive index spectrum of Mode 4 particles.

To simplify the retrieval problem the initial retrievals are performed by assuming 4 narrow particle size distributions. The assumed log-normal size distributions have a geometric mean radius (R_0) of 0.3, 0.5, 1, 2, μm and a geometric standard deviation (σ_0) of 0.05. Then, the NEMESIS is set to retrieve a vertical abundance profile of the Mode 4 particles. The a priori vertical abundance profile is assumed constant with altitude and equal to 10^{-5} particles/g along with an error of 100% (shown by the dotted line and shaded area in Figures 11a and 11b). Thus, NEMESIS is free to retrieve a continuous profile of mode 4 particle abundance. A correlation length of 1 km is assumed on this profile since the Format I radiance profiles have an average vertical resolution of 0.5 km. Starting with a conservative approach, Rayleigh scattering Model A is used for initial retrievals. The vertical abundance retrievals should show a nearly constant vertical profile if there is a uniformly dispersed haze while a peak in profile should occur if there is a detached particulate layer.

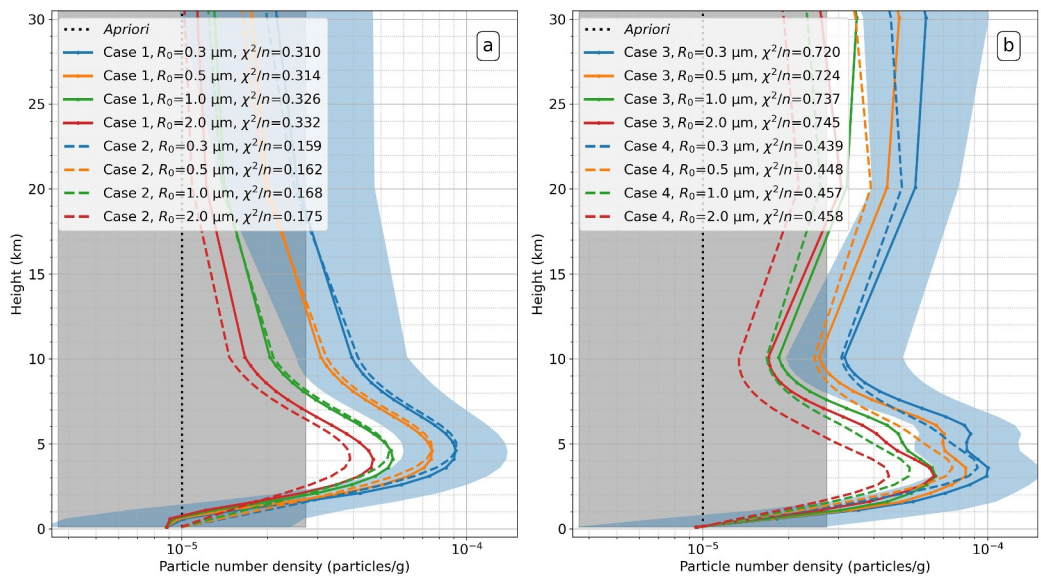

Figure 11. (a) The retrieved abundances of the mode 4 particles for Case 1 (solid lines) and Case 2 (dashed lines), (b) the same for Case 3 (solid lines) and Case 4 (dashed lines). For each case, retrievals using different mean radii (0.3–2 μm) of Mode 4 particles are shown by different colors. The legend also includes the spectral fits (χ^2/n). The retrievals use Rayleigh scattering Model A. The dotted black line shows the a priori abundance profile. The shaded areas represent the a priori or a posteriori errors.

The surface of Venus appears to be largely basaltic and windblown dust particles are one of the candidates for NSPL. Thus, as a starting point, the values of the real (η_r) and imaginary (η_i) parts of the refractive index are chosen to match basaltic particles from Pollack et al. (1973). The η_r was assumed to be 1.5 at 0.63 μm and the a priori estimate of η_i is chosen as 10^{-3} with 100% error. Since the layering scheme was changed to have a lower resolution in the clouds, the estimation of extinction caused by the clouds is also affected. Thus, we re-retrieve the scaling factors on the four particle modes of MCD. As we already have a good estimation of the abundance of the particle modes in MCD a tighter constraint of 50% a priori error is now used. A total of 16 retrievals are run, using the four assumed particle size distributions and the four cases of the radiance profiles given in Section 3.6.

Cases 1 and 2 use the Format I radiance profiles from 30 km down to 0 and 1.86 km, respectively (Section 3.6). The input spectra are provided at the base altitudes of the altitude grid following the Layering Scheme 2 (section Appendix A). Thus, a total of 23 spectra (for altitude points between 30 and 0 km) and 19 spectra (for altitude points between 30 and 1.86 km) are used as the input for cases 1 and 2, respectively. The two cases were chosen to determine the effect of the change of scale of the x-axis on the original graphs. Figure 11a shows the retrieved abundance profiles by solid and dashed lines for Cases 1 and 2, respectively. It can be observed that both cases produce similar abundance retrievals with Case 1 abundance peaking at ≈4.5 km and Case 2 abundance peaking at ≈5 km. An a posteriori error of ≈40%–42% was obtained at the peak altitudes for both cases (shown for only Case 1, $R_0 = 0.3$ μm retrievals in Figure 11a to improve readability). The peak in abundance profile retrievals could still be distinguished despite the magnitude of the a posteriori error. The slight difference in the peak altitude could be explained based on the difference in the bottom altitude of Case 1 and 2 radiance profiles. However, the similarity in retrievals for each of the particle distributions of both cases indicates that the change of scale of the x-axis at 3500 s (1.86 km) on the original graphs (e.g., Figure 1) has not severely affected retrievals of Mode 4 particle abundance. Also, the Case 2 retrievals show slightly better χ^2/n values (0.16) than Case 1 $\left(\chi^2/n = 0.31\right)$. For Case 1, the change of slope at ≈1 km worsens the fits in the lowest 1 km. Since there is no radiance data below 1.86 km in Case 2 the χ^2/n values are better.

Cases 3 and 4 use the Format 0 binned radiance profiles with altitude bins of 0.5 and 1 km respectively. Here, the input spectra are provided at the centre of the respective altitude bins. Thus, a total of 60 and 30 spectra between the altitude of 30 to 0 km are given as the inputs for cases 3 and 4, respectively. As explained in Section 3.6, the bins where no Format 0 data is present are filled with a linearly interpolated value and an accompanying error of 100% to ensure that NEMESIS does not prioritize fitting these points. These two cases were selected to study (a) the effect of graphical artefacts from Format I data on abundance retrievals and (b) the effect of binning size on Format 0 data. In Figure 11b, Case 3 (solid lines) shows a double peak structure in the Mode 4 abundance profile with a primary peak of 3.5 km and a secondary peak at 5.5 km, while Case 4 (dashed lines) shows a single peak at an altitude of 3.5 km. Moshkin et al. (1983) stated that the original $I_s\downarrow$ radiance, which is the Format 0 data, had more random error than the I_w data (Section 2.4). Thus, the double peak structure retrieved from Case 3 profiles could be a retrieval artefact. Similar to cases 1 and 2, an a posteriori error of ≈40%–45% is obtained on the Mode 4 abundance profile at the peak altitudes for cases 3 and 4. While the magnitude of a posteriori error is sufficient to distinguish a peak in retrievals, it is not small enough to support the double peak structure. Also, the larger bin size used in Case 4 resulted in the smoothing of the radiance profile and subsequent retrievals showed a single peak. Based on this, while a peak could be clearly distinguished from both cases, the double peak structure from Case 3 is likely to be a retrieval artefact. Next, the χ^2/n values of Case 3 (≈0.72) are greater than Case 4 (≈0.45). This implies that the smoothing due to the larger bin size also improves the fits (lowers the χ^2/n values). Thus, the single peak retrieved from Case 4 radiance profiles further supports abundance retrievals from Cases 1 and 2 (i.e., the Format I radiance profiles). Lastly, the abundance retrievals from Cases 3 and 4 also hint at a uniformly dispersed particulate layer from 30 to 20 km in the atmosphere. This needs further investigation that could be treated as a separate study.

For comparison with the test runs without added extinction in the atmosphere (Runs A and B from Section 5.1), Run C in Figure 10 shows the fitted profiles from the Case 3 retrievals with a Mode 4 size distribution of $R_0 = 0.5$ μm and $\sigma_0 = 0.05$ μm. The better fits from Run C (solid line) are directly noticeable. For all 4 cases and all assumed particle sizes, the retrievals consistently show a pronounced layer in the lowest 10 km. This indicates that the change of slope at ≈1 km and the change of scale at 1.86 km have not significantly affected the Mode 4 retrievals for the assumed choice of vertical grid cell size (0.5 km) and correlation length (1 km). The χ^2/n values are lower than 1 for all the retrievals including retrieved NSPL which strongly supports the presence of a near-

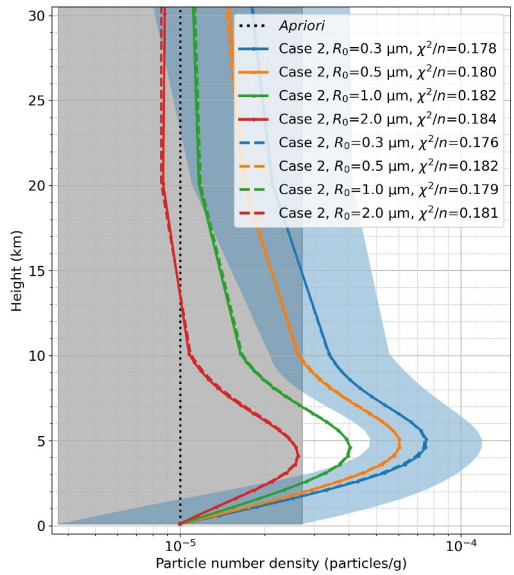

Figure 12. The retrieved abundances of the mode 4 particles for Case 2 radiance profiles. The solid lines represent the retrievals using Rayleigh scattering Model B, while the dashed lines show the retrievals using Rayleigh scattering Model C. Retrievals using different mean radii (0.3–2 μm) of Mode 4 particles are shown by different colors. The legend also includes the spectral fits (χ^2/n). The dotted black line shows the a priori abundance profile. The shaded areas represent the a priori or a posteriori errors.

surface particulate layer at the time and location of Venera 13 landing. For all 4 Cases, χ^2/n values slightly decrease with the particle size. Thus, retrievals favor the idea of smaller sub-micron particles.

Next, the retrievals are repeated for Rayleigh scattering Models B and C using only the Case 2 radiance profiles and other parameters are kept the same as before. In Figure 12 the Mode 4 abundance retrievals using Models B and C are shown by solid and dashed lines respectively. Comparing with the Model A and Case 2 retrievals from Figure 11a, a drop in the peak abundance can be observed while the altitude of peak abundance remains the same. The drop in the peak abundance is due to the added optical thickness from Rayleigh scattering Models B and C as compared with Model A. As discussed in Section 4.3, Model C included a hypothesized composition gradient in the atmosphere below 7 km. While Model C further adds a very small amount of optical thickness below 7 km as compared with Model B, not much difference can be observed in the mode 4 retrievals using both. Based on this, the Rayleigh scattering Model C is not considered for further retrievals.

Using the Venera 13 Format I data, an extinction profile was retrieved by Grieger et al. (2004) that shows a sharp primary peak approximately between 1.3 and 1.9 km altitude, centered at ≈1.5 km altitude along with a secondary diffused peak approximately between 4 and 8 km altitude, centered at ≈5 km altitude. The peak altitude in our retrievals matches with the secondary peak from Grieger et al. (2004), but not with the primary peak at ≈1.5 km. This difference in both results could be attributed to the differences in retrieval methodology. We have not used Format I upward radiance profiles as they were affected by the thermal noise in the lowest 7 km (as explained in Section 3). Whereas, Grieger et al. (2004) used both the downward and upward radiance profiles. Thus, to check the effect of upward radiance profiles, we repeated the retrievals using both the upward and downward radiance profiles (Case 1). The mode 4 retrievals showed a single peak at 1.5 km, matching the altitude of the primary peak retrieved by Grieger et al. (2004). However, the use of upward radiance profiles resulted in considerably worse spectral fits of $\chi^2/n \approx 12$. Along with the use of upward radiance profiles, differences in modeling parameters like the vertical grid cell size could have also contributed to the difference in both results.

5.3. Size and Refractive Index of the Mode 4 Particles

To further constrain the particle size, NEMESIS was set up to retrieve the geometric mean radius (R_0) along with other parameters retrieved earlier. A log-normal size distribution was assumed and 10 particle sizes (0.3, 0.5, 0.75, 1, 2, 3, 4, 5, and 10 μm) were used as a priori values of (R_0). The a priori error (ν_{R_0}) was kept at 100% so that the NEMESIS is free to retrieve R_0 under the log-normal parameterization. At the same time, the value for geometric standard deviation (σ) was kept fixed. Based on the values for Modes 1 to 3 in the MCD, the σ was assumed to be 0.25.

The Case 2 radiance profiles previously provided the best fit among the four Cases, so they are now used as the input to NEMESIS. A fairly low value of $\chi^2/n = 0.16$ was previously achieved for the retrievals with Case 2 profiles. This meant that the simulated radiance profiles were in very good agreement and much within the 10% measurement error on the assumed on the Case 2 radiance profiles. In this step, the error on the measured profile was further reduced to 5% to fit the simulated radiance profiles even more closely with the measured radiance profiles.

Fifteen real refractive indices ($\eta_{r@0.63\mu m} = 1.1, 1.2, \ldots$up to 2.5) were considered. The rest of the real refractive index spectrum was reconstructed using the Kramers–Kronig approximation. The a priori η_i was considered to be 0.001 throughout with an a priori error of 100%. The correlation length of 0.05 μm (twice the FWHM of the IOAV-2 spectral channels) was used for η_i retrievals. As discussed in the previous section, the retrievals are now carried out using both the Rayleigh scattering Models A and B. Thus, a total of 150 retrievals (10 mean particle sizes (R_0) × 15 η_r) were performed for each of the Rayleigh scattering Models (A and B). Out of these, 9 retrievals

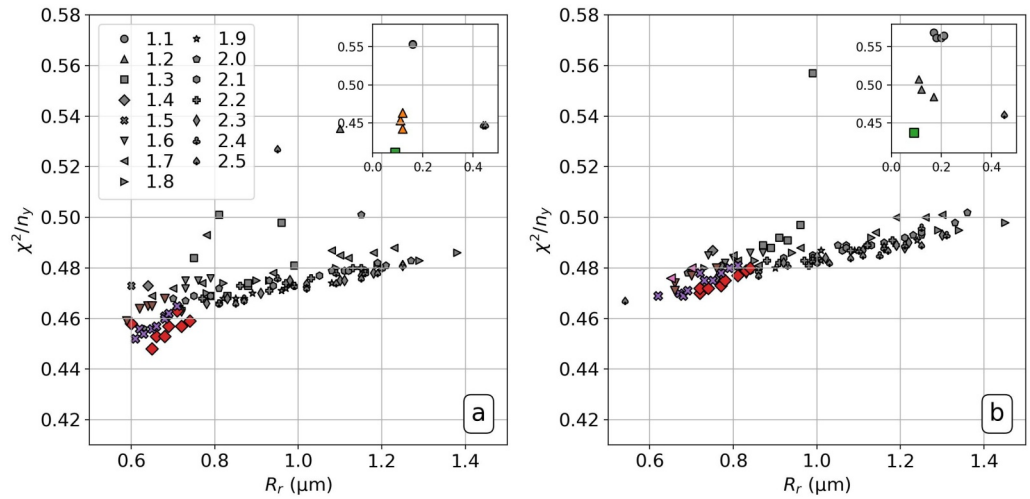

Figure 13. Scatter plots of χ^2/n versus the retrieved mean particle radius (R_r). Subfigures (a, b) represent the use of Rayleigh scattering Models A and B, respectively. The legend shows different makers that indicate different $\eta_{r@0.63\mu m}$ (from 1.1 to 2.5). The colored markers indicate the selected retrievals where the χ^2/n and a posteriori errors on R_r (ν_{R_r}) are below the threshold described in the text. The gray markers show the rest of the retrievals that have been filtered out.

with Model A and 10 retrievals with Model B, showed inconsistent retrievals with either the $\chi^2/n > 1$ or $R_r > 2$. These outliers were removed and the remaining retrievals were considered for further analysis. All 141 retrievals with Model A and 140 retrievals with Model B provide valid solutions ($\chi^2/n < 1$) which highlights the level of degeneracy and hence, the difficulty behind direct retrievals of particle size and η_i.

The valid retrievals show a range of show a range of χ^2/n values. For Model A, the χ^2/n ranges from 0.411 to 0.717, while for Model B it ranges from 0.437 to 0.951. Similarly, the a posteriori errors on R_r (ν_{R_r}) range from 22.22% to 52.74% for Model A and those for Model B range from 23.75% to 53.37%. To refine the analysis, a threshold is established at the 30 percentile mark for both the χ^2/n and ν_{R_r}. For Model A, the threshold values are $\chi^2/n = 0.469$ and $\nu_{R_r} = 29.93\%$. Similarly, for Model B, the threshold values are $\chi^2/n = 0.481$ and $\nu_{R_r} = 31.23\%$. The retrievals with both χ^2/n and ν_{R_r} below the threshold are selected for further analysis and the retrievals above the threshold are filtered out.

Figure 13 shows scatter plots of χ^2/n versus R_r for Models A and B, with different markers indicating different values of $\eta_{r@0.63\mu m}$ from 1.1 to 2.5. The markers highlighted with colors show the above-selected retrievals while the markers in gray color indicate the retrievals that are filtered out. It can be observed that the highlighted retrievals also coincide with a minimum in the values of χ^2/n for both the Rayleigh scattering models (for $0.5 < R_r < 1.5$). For model A, 8 out of 10 retrievals for $\eta_r = 1.4$, 9 retrievals for $\eta_r = 1.5$, and 5 retrievals for $\eta_r = 1.6$ lie inside the minimum. Similarly, for Rayleigh scattering model B, 8 retrievals for $\eta_r = 1.4$, all 10 retrievals for $\eta_r = 1.5$, and 4 retrievals for $\eta_r = 1.6$ lie inside the minimum. The a priori mean particle radius (R_0) ranges from 0.3 to 10 μm while all the retrievals with $\eta_r = 1.4$, 1.5, and 1.6 consistently show a retrieved mean particle radius in the range of $0.6 < R_r < 0.85$ μm, for both the Rayleigh scattering Models. Based on this, the selected retrievals lying inside the highlighted minimum are termed as the best-fit set of retrievals. Despite the degeneracy, the best-fit set suggests that the Mode 4 particles could have $\eta_{r@0.63\mu m}$ around 1.4 to 1.6 with the range of mean particle radius R_r between 0.6 and 0.85 μm (with a maximum of ≈31% error).

Next, two retrievals from Model B with $\eta_r = 1.7$, also lie below the threshold with $R_r = 0.65$ and 0.7 μm. However, the rest retrievals with $\eta_r = 1.7$ show a bigger range R_r from 0.8 to 1.3 μm. Due to a larger spread of the R_r values, the retrievals with $\eta_r = 1.7$ are not considered any further. Moreover, 10 retrievals each from models A and B show $0 < R_r < 0.5$. They are shown within the insets in Figure 13. For Model A, 3 retrievals with $\eta_r = 1.2$, and 1 retrievals with $\eta_r = 1.3$ and for Model B, 1 retrievals with $\eta_r = 1.3$ falls within the threshold values for χ^2/n and ν_{R_r}. These retrievals have R_r values in the range of 0.09–0.12. However, the rest of the retrievals from $\eta_r = 1.2$ and 1.3 show a wide range of R_r, that is, 0.79 to 1.4 μm. Since the retrievals with $\eta_r = 1.2$ and 1.3 do not show

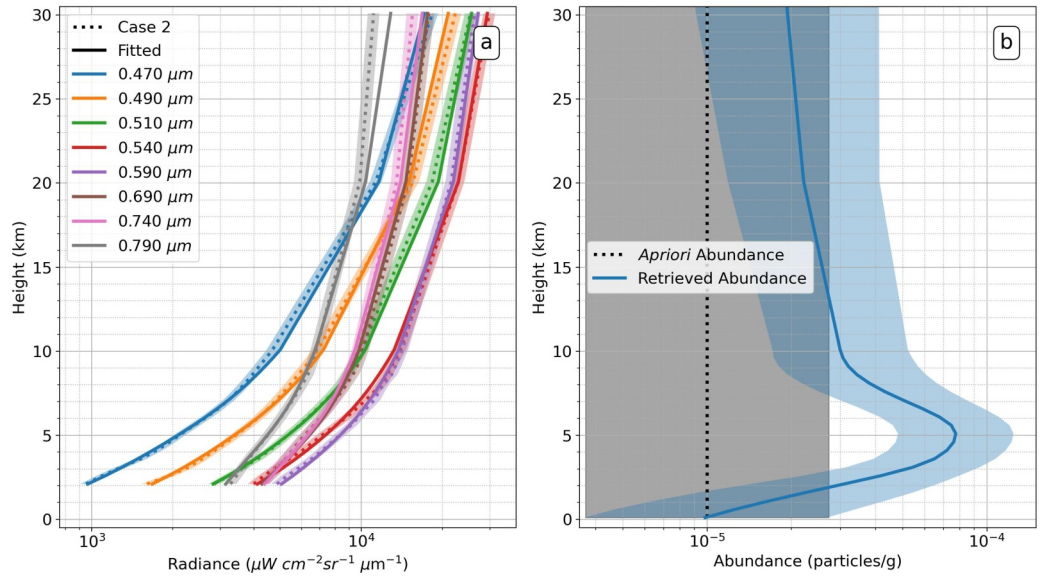

Figure 14. (a) Fitted radiance profiles (solid lines) for the example retrieval discussed in the text ($\eta_{r@0.63\mu m} = 1.4$, $R_r = 0.69$ μm). The dotted lines represent the Case 2 profiles and the corresponding shaded area shows the estimated measurement error. Different colors indicate different wavelengths. (b) The retrieved abundance profile of Mode 4 particles (solid blue line) from the same example. Here, the a priori abundance profile is shown by the dotted black line. The shaded areas represent the corresponding a priori or a posteriori errors.

consistency in the values of R_r, as opposed to the best-fit set, they are not considered any further. Lastly, two retrievals each from Rayleigh scattering models A and B show $1.5 < R_r < 2$. However, their χ^2/n and ν_{R_r} values are above the threshold hence they are filtered out and not shown in Figure 13.

An example from the best-fit set is discussed next. This retrieval run used Model A, $\eta_{r@0.63\mu m} = 1.4$ and $R_0 = 2$ μm while the R_r obtained was 0.69 μm. A $\chi^2/n = 0.457$ is obtained for this retrieval. As shown in Figure 14a, the fitted radiance profiles are well within the assumed measurement error of the Case 2 radiance profiles used as the input. The corresponding Mode 4 abundance retrieval is shown in Figure 14b. The NSPL peaks at 5 km altitude, with a peak abundance of 7.7×10^{-5} particles/g. This profile is similar to the abundance retrievals shown in Figure 11a that used Case 1 and 2 radiance profiles but with a fixed R_0. The best-fit set of retrievals from Model A show similar abundance profiles with an average Mode 4 column optical thickness at 0.63 μm, $\tau_{total@0.63\mu m}$ ranging from 2.66 to 4.10. As discussed in Section 5.2, Model B shows a lower peak abundance but a similar peak altitude for Mode 4 particles. The best-fit retrievals from Model B show a Mode 4 column optical thickness, $\tau_{total@0.63\mu m}$ in the range of 1.88–3.39.

The retrieved imaginary refractive index (η_i) spectrum for the above example is shown in Figure 15. While the a priori η_i was kept constant throughout and equal to 0.001, the broad features like the peaks at 0.47 and 0.7 μm and the troughs at 0.59 and 0.79 μm were retrieved by NEMESIS with the a posteriori errors around 25%. Similar features are present in all best-fit retrievals. The corresponding single scattering albedo (ϖ) along with the a posteriori errors is shown in Figure 16. The Mode 4 particles are more absorbing at 0.47 μm with the $\varpi = 0.96$ and the absorption steadily decreases till 0.79 μm with a brief increase in between from 0.59 to 0.69 μm. Beyond ≈0.75 μm ϖ becomes greater than 0.99 which means the particles are mainly scattering.

Figure 16 also shows the retrieved ϖ of Mode 1 particles from Section 4.5. Since, Modes 2, 2′, and 3 have $\varpi >$ 0.9999 and can be considered as fully scattering throughout the wavelength range in consideration (0.47–0.79 μm), they are not plotted in this figure. The previously retrieved Mode 1 ϖ spectrum shows a similar shape with lower absorption than the Mode 4 particles. Also for Mode 1, the $\eta_{r@0.63\mu m} = 1.43698$ (as per Palmer and Williams (1975)) which lies within the estimated range η_r for Mode 4 which 1.4 to 1.6. Here, it could be very tempting to assume that both particles could be composed of a similar material. However, it should be noted that the retrieved Mode 1 ϖ was guided to adopt the current shape by constraining a priori η_i spectrum (Section 3.6),

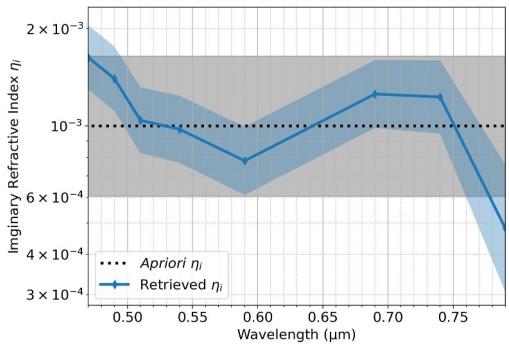

Figure 15. The retrieved η_i spectrum of Mode 4 particles (solid line) for the example retrieval discussed in the text ($\eta_{r@0.63\mu m} = 1.4$, $R_r = 0.69$ μm). The a priori η_i is shown by the dotted line. The shaded areas represent the corresponding a priori or a posteriori error.

whereas Mode 4 ϖ retrievals were completely free from such constraints. Also, while Mode 4 is present in the lowest 10 km, Mode 1 is higher up in the atmosphere (≈48–85 km) and the pressure-temperature regimes for both Modes differ drastically. Based on this, it is less likely that both Modes have a common origin and more work is required to find a formation mechanism that could simultaneously explain the presence of both Modes at different altitudes.

6. Discussion

The previous section presented the best-fit set of retrievals for mean particle size and refractive indices of the NSPL. Now, it is important to understand what these constraints mean for the nature of the near-surface particulates. Previous authors have suggested that a near-surface particulate layer could be formed due to aeolian lofted surface material, volcanic ash or even condensing volatiles. The dense atmosphere of Venus provides dynamic conditions for aeolian transport between those of terrestrial subaerial and subaqueous environments. Although an active transport has not been directly detected within the existing data, resolved and unresolved aeolian bedforms are globally present (Kreslavsly & Bondarenko, 2017). While the impact craters appear to be the largest source of sediments, fine-grained material is also present at various volcanic sites (Carter et al., 2023). Thus, there is ample evidence to suggest substantial transport of material through wind. The dynamics simulations performed by Lefèvre (2022) show a convective boundary layer reaching up to 7 km above the highlands (Ovda Regio), with the surface wind being strong enough to uplift the dust particles up to this level. Also, the previous in situ measurements suggest that much of the surface is primarily basaltic (Gilmore et al., 2023). Lastly, within the wavelength range of 0.48–0.8 μm, typical basaltic values of η_r ≈1.52 and $\eta_i \approx 10^{-3}$ (Pollack et al., 1973) match well the retrieved refractive index properties of the NSPL. This suggests that the NSPL could have been formed due to the sediments uplifted from the surface.

Volcanic ash forms another candidate for the near-surface particulates. It is widely known that the surface of Venus is covered in volcanoes (Hahn & Byrne, 2023; Herrick et al., 2023) and there is some evidence of active volcanism during recent times (Herrick & Hensley, 2023; S. E. Smrekar et al., 2010). In the case of explosive eruptions, along with the gases, fine volcanic ash particles could also be lofted into the atmosphere (Wilson et al., 2024). Since no direct measurements of volcanic ash particles are available from Venus, reference can be taken from the volcanic ash aerosols ejected by various volcanoes on Earth. For example, the volcanic ash samples from the eruption of Mount Eyjafjallajökull, Iceland, in 2010; Mount Tongariro, New Zealand, in 2012; Mount Augustine, Alaska, in 2006; Mount Chaitén, Chile, in 2008; show η_r in the range of 1.51–1.53, while η_i measurements show a wider range from 10^{-6} to 10^{-3} (Ball et al., 2015; Reed et al., 2018). At the same time, some other eruptions like Mount Calbuco, Chile, in 2015; Mount Grímsvötn, Iceland, in 2011; and Mount Etna, Italy, in 2017; show η_r to be in the range of 1.59–1.63 with η_i measurements in the range of 10^{-4} to 10^{-3}(Deguine et al., 2020). The above η_r values are consistent with the NSPL retrievals while the η_i values seem to have more uncertainty between measurements. Nevertheless, the omnipresence of volcanos on the surface of Venus along with the evidence of recently active volcanism make volcanic ash another strong candidate for the near-surface particulates.

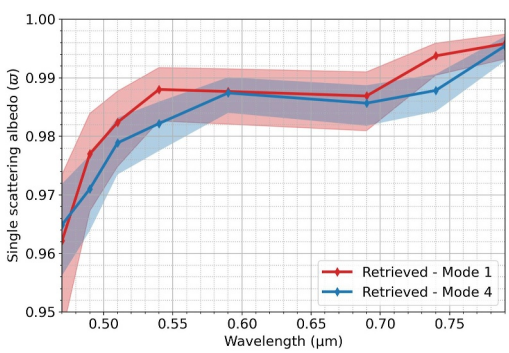

Figure 16. The retrieved ϖ spectrum of Mode 4 particles (blue line) for the example retrieval discussed in the text ($\eta_{r@0.63\mu m} = 1.4$, $R_r = 0.69$ μm). The red line shows the retrieved ϖ spectrum of the MCD Mode 1 particle ($R = 0.30$ μm and $\sigma = 0.44$ μm). The shaded areas represent the a posteriori error.

Brackett et al. (1995) demonstrated that diffusive migration of metal halides and chalcogenides at rates of 0.01 to >10 μm/yr could occur from Venusian lowlands to highlands. They also suggested that the presence of such volatile phases could have been responsible for the anomaly encountered by all four Pioneer Venus at 12.5 km and the haze encountered by Pioneer Venus Night and North Probes. Similarly, Grieger et al. (2004) suggested that the NSPL could be related to the species forming the "radar snow." Radar snow is a term used to indicate a sudden increase in radar albedo observed at some highlands on Venus (Pettengill et al., 1992). The critical altitude at which

this change occurs varies from 1.49 km at Sapas Mons to 3.75 km at Maxwell Mons (Klose et al., 1992). The Maxwell Montes extend up to ≈10 km and exhibit the phenomenon of "radar snow" up to the top, which suggests that the compound behind its formation should be present in the atmosphere and stable at altitudes up ≈10 km. Thus, the transport of volatile vapors could be responsible for the formation of a layer peaking at ≈5 km altitude. Semiconductor species like Tellurium (Te), Galena (PbS), Bismuthite (Bi_2S_3), Bismuth Telluride (Bi_2Te_3) and Mercury Telluride (HgTe) have been previously suggested as the likely candidates for the radar snow (Kohler et al., 2015; Pettengill et al., 1996; Schaefer & Fegley, 2004). For Tellurium, the refractive indices of thin films (Ciesielski et al., 2018) show a value of $\eta_{r@0.4\mu m} = 1.06$ increasing to $\eta_{r@0.8\mu m} = 3.4$ and $\eta_{i@0.4\mu m} = 2.15$ to $\eta_{i@0.8\mu m} = 2.42$. Here, it should be noted that the thickness of the thin films used for measurement was too small (20–30 nm thick) as compared with the retrieved particle size. Thus, the optical properties could be different than those for a sphere of ≈0.8 μm radius. Mahmoud et al. (1997) provide the optical properties of Bismuthite for films with a thickness of 0.5 μm heated to 453 K. The $\eta_{r@0.59\mu m} = 1.9$ increases to $\eta_{r@0.8\mu m} = 2$ and $\eta_{i@0.4\mu m} = 0.37$ increases to $\eta_{i@0.8\mu m} = 0.67$. Next, Galena shows a value of $\eta_{r@0.5893\mu m}$ and $\eta_{r@3\mu m} = 4$ (Ravindra & Srivastava, 1982). The Bismuth Telluride shows a high value of the refractive index with $\eta_{r@0.4\mu m} \approx 4.5$ sharply increasing to $\eta_{r@0.8\mu m} \approx 6.7$ (Mico et al., 2019). Lastly, the Mercury Telluride shows a refractive index of $\eta_r \approx 3$ to 4 for the bulk material and $\eta_r \approx 2.35$ for thin films (Rastogi et al., 2021).Thus, no direct match could be found between the refractive indices retrieved above and the prominent candidates for volatile transport on Venus.

The above arguments suggest that basaltic dust lifted from the surface is consistent with the retrieved properties of the NSPL. At the same time, there is a good possibility that the particles could be volcanic. Also, the comparison of refractive indices suggests that it is less likely that NSPL could originate from the volatile condensates. An approximate settling velocity calculation for a basalt sphere of radius 0.8 μm floating at 5 km altitude in the atmosphere of Venus gives a settling velocity of ≈ 70 m/week (see Appendix B). In other words, it would take ≈1.4 Earth years for the NSPL layer to settle down from an altitude of 5 km to the surface. This also suggests that we should not expect such layers to be the same between missions conducted more than a couple of years apart. Here, dynamic simulations focusing on the near-surface atmosphere are required to understand the nature of the uplifting event and a more accurate calculation of the settling velocity of the particulates. In this way, we have analyzed the last of the in situ spectrophotometric observations of the atmosphere of Venus. While VenDI/DAVINCI will perform in situ imaging observation in one narrowband and one wideband near-IR channel (Garvin et al., 2022), new in situ spectrophotometric observations in the visible range are required to learn more about deep atmospheric phenomena like the NSPL.

7. Conclusion

The extreme conditions in Venus' deep atmosphere create difficulties for in situ missions. The data recorded by the past in situ missions showed inconsistent evidence regarding the existence of a near-surface particulate layer (NSPL). To investigate this further, we have reconstructed a part of the lost Venera 13 spectrophotometric data set using the original graphic material and categorized it into three formats. Format 0 contains the digitized version of calibrated radiance data points printed on the original graphs. Format I contains the smooth radiance profiles that were (hand) drawn on original graphs through the printed radiance data points from 62 km down to the surface. These smooth profiles were later corrected, averaged vertically and presented in the form of spectra at 11 altitude points by Moshkin et al. (1983). These corrected spectra form the Format II of the reconstructed data set. The Format I data set is used for retrievals in this study since a high vertical resolution is required to resolve the minute changes in the radiance profile necessary to retrieve a narrow particulate layer. Format 0 and II data sets are used for the estimation of digitization and graphical artefacts and their effects on the retrievals. The following effects are observed in the Format I data set:

1. Comparing the Format I and Format II data on a common grid, we find that the data sets are not exactly consistent with each other, due to additional radiometric recalibration of Format II data. Various effects were observed in the Format I data, including thermal noise in the upward radiances, and distortion longward of 0.8 μm.
2. Out of Venera 13 upward and downward data, the first eight Venera 13 Format I downward radiance profiles till 0.8 μm were deemed to be the least affected and are further used in this paper.
3. A deeper inspection of the original graphs and Format 0 data revealed two important graphical artefacts—(a) a scale change at 1.86 km altitude and (b) excessive smoothing causing a slope change as compared to the

Format 0 data at 1 km altitude in Format I data. Both of these effects contributed to a sudden change of slope for all the radiance profiles below 1.86 km. To check if these graphical artefacts could affect the aerosol retrievals, 4 cases of the selected radiance profiles were considered: (a) Format-I Profiles till 0 km, (b) Format I Profiles till 1.86 km, (c) Format 0 Binned Profiles with altitude bins of 0.5 km, (d) Format 0 Binned Profiles with altitude bins of 1.0 km.

Using NEMESIS, a radiative transfer and retrieval tool, the model atmosphere was first updated with the local conditions of the Main Cloud Deck (MCD) at the time of the Venera 13 landing. The Venera 13 Format I radiance profiles from 60 to 30 km altitude were used for this. The cloud base was found to be at ≈49 km and the abundances of 4 particle modes (1, 2, 2′, and 3) along with the imaginary refractive index spectrum of the Mode 1 cloud particles were retrieved. Then various simulations and retrievals were performed while fitting the radiance data below 30 km and their outcomes are summarized below:

1. Initial forward runs were performed to check the possibility that no particulate matter exists below 10 km. These simulations suggested another source of extinction is required in the atmosphere to fit the radiance data within the assigned error bars.
2. New particles, termed Mode 4, were then introduced into the updated model atmosphere. Different retrievals were set up by assuming 4 different radii for these particles. The a priori abundance for the Mode 4 particles was assumed to be vertically constant. The radiance profiles from the 4 Cases discussed earlier are used for retrievals. The results from all 16 retrievals (4 particle radii x 4 Cases of radiance profiles) produced a peak in the Mode 4 abundance profile in the lowest 10 km with peaks at 4.5, 5, 3.5, and 3.5 km for the four Cases of radiance profiles respectively. The magnitude of peak abundance was similar for all four radiance cases which suggested that the graphical artefacts due to the change of scale on the original graphs and excessive smoothing slightly affected the altitude of peak abundance, but did not significantly alter the magnitude of the peak abundance. In this way, the consistent retrievals of a peak in the abundance profiles for various cases strongly support the presence of the NSPL in the atmosphere.
3. The deep atmospheric retrievals are sensitive to Rayleigh scattering. To consider all possibilities different Rayleigh scattering models were tested. It was noted that the Rayleigh scattering model producing higher optical thickness resulted in a slight reduction in the retrieved mode 4 abundance. The hypothesis of a CO_2-N_2 composition gradient in the lowest 7 km (Lebonnois & Schubert, 2017) was also tested. However, it did not have any considerable effect on the retrievals.
4. The extinction profiles retrieved by Grieger et al. (2004) using the Format I upward and downward radiances, show a sharp primary peak at 1.5 km and a broad secondary peak at 5 km. Our retrievals show a peak in Mode 4 abundance at ≈5 km but do not indicate a sharp primary peak at 1.5 km. Based on simulations, the most probable reason for this difference is the use of only downward radiance profiles in our retrievals as compared to the upward and downward radiance profiles used by Grieger et al. (2004).
5. To constrain the Mode 4 particle size and the real refractive index, retrievals were carried out using ten a priori log-normal particle size distributions (with the mean particle radii going from 0.3 to 10 μm and a standard distribution of 0.25) and fifteen values of real refractive index at 0.63 μm (η_r) from 1.1, 1.2…up to 2.5. Also, two different Rayleigh scattering models are considered. Out of the 300 retrievals, the most probable Mode 4 particles were selected by putting a threshold on radiance fits $\left(\chi^2/n\right)$ and a posteriori error on retrieved radii (V_{R_r}), and looking at the range of retrieved particle radii (R_r) for a given η_r. The best-fit set of retrievals had a range of $\eta_r = 1.4$ to 1.6 and consistently retrieved the mean particle radii (R_r) between 0.6 and 0.85 μm with a maximum of 31% a posteriori error along with retrieved imaginary refractive index (η_i) values $\approx 10^{-3}$. The above range of parameters could be used as the first constraint on the particles forming the near-surface particulate layer.
6. The retrievals suggest 1.4 to 1.6 as the probable range of η_r which matches well with the η_r of basalt particles (≈1.52). The magnitude of retrieved η_i also matches well that of basalt particles. Since there is good evidence of sediment transport and aeolian activity over the surface of Venus which is largely covered by basaltic rock, the retrieved NSPL could likely be formed due to basaltic dust lifted from the surface. Alternatively, the measured η_r values are also consistent with the measured η_r values of volcanic ash samples collected from some terrestrial volcanoes (1.51–1.53, 1.59–1.63). Also, the Venusian surface shows plenty of volcanic sites and there is some evidence of recently active volcanism. Based on this, the volcanic ash is another strong candidate for the formation of NSPL. The third mechanism that could be responsible for the formation of the NSPL could be the transport of volatile vapors from hot lowlands to colder highlands. However, the available

refractive indices of prominent candidates for volatile vapors do not match with the retrievals. While this makes the volatile vapors less likely to be responsible for the formation of the NSPL, more study is required to identify suitable candidates and their properties.

Appendix A: The Base Altitudes of the Layering Schemes

In this work we have discussed two different types of retrievals: (a) main cloud deck (MCD) retrievals and (b) Near-surface retrievals. However, NEMESIS supports up to only 39 atmospheric layers for scattering calculations. Thus, for both types of retrievals different layering schemes are used that have a finer altitude grid in the region of interest and a coarser altitude grid elsewhere. Layering Scheme 1 corresponds to MCD retrievals and Layering Scheme 2 corresponds to near-surface retrievals. Table A1 lists the base altitudes for both the layering schemes. The altitudes are with respect to a mean planetary radius of 6,052 km.

Table A1
Base Altitudes for Layering Schemes 1 and 2

Layer no.	Scheme 1 base altitudes (km)	Scheme 2 base altitudes (km)
1	0.1	0.1
2	5.1	0.6
3	10.1	1.1
4	15.1	1.6
5	20.1	2.1
6	25.1	2.6
7	30.1	3.1
8	35.1	3.6
9	40.1	4.1
10	45.1	4.6
11	46.1	5.1
12	46.6	5.6
13	47.1	6.1
14	47.6	6.6
15	48.1	7.1
16	48.6	7.6
17	49.1	8.1
18	49.6	8.6
19	50.1	9.1
20	51.1	9.6
21	52.1	10.1
22	53.1	20.1
23	54.1	30.1
24	55.1	45.1
25	56.1	46.1
26	57.1	46.6
27	58.1	47.1
28	59.1	49.1
29	60.1	49.6
30	61.1	50.1
31	62.1	55.1
32	63.1	60.1

Table A1
Continued

Layer no.	Scheme 1 base altitudes (km)	Scheme 2 base altitudes (km)
33	65.1	65.1
34	70.1	70.1
35	75.1	75.1
36	80.1	80.1
37	85.1	85.1
38	90.1	90.1
39	95.1	95.1

Appendix B: Calculation of Settling Velocity in the Laminar Region

The settling velocity v is the constant velocity attained by the particle as it falls through the fluid under the influence of gravity. It is reached when the gravitational force acting on the particle balances the viscous drag exerted by the fluid. Within the laminar flow regime, v of a small spherical particle in a fluid can be calculated using Stokes' Law as shown below:

$$v = \frac{2}{9}\frac{r^2\left(\rho_p - \rho_f\right)g}{\eta} \tag{B1}$$

where:

- v is the settling velocity (m/s),
- r is the radius of the particle (m),
- ρ_p is the density of the particle (kg/m^3),
- ρ_f is the density of the fluid (kg/m^3),
- g is the acceleration due to gravity (m/s^2),
- μ is the dynamic viscosity of the fluid (N-s/m^2).

At the height of 5 km in the atmosphere of Venus, $\mu = 3.05 \cdot 10^{-5}$ N-s/m^2 (Schiffer et al., 1968), $g = 8.855$ m/s^2 and $\rho_f = 49.87$ kg/m^3 (Seiff et al., 1985). For a basalt particle of $r = 0.8$ μm and $\rho_p = 2{,}900$ kg/m^3, this gives $v = 71.18$ m/week. Assuming that the values of g, ρ_f and μ remain constant from 5 km altitude to the surface, it can be said that the particles will settle down from 5 km altitude to the surface in 491.74 Earth days or 1.34 Earth years.

Data Availability Statement

The Venera 13 spectrophotometric reconstructed data sets (Format 0, I, II) used in this study are available from N. Ignatiev and Kulkarni (2024). The spectral fitting and retrievals were performed using the NEMESIS radiative transfer and retrieval algorithm (P. G. J. Irwin et al., 2008) and can be downloaded from P. G. J. Irwin et al. (2022a), with supporting website information at P. G. J. Irwin et al. (2022b). The data products supporting all the figures in this study are available from Kulkarni et al. (2024).

Acknowledgments
We are grateful to the United Kingdom Science and Technology Facilities Council for funding this research through a PhD Studentship (Grant No. ST/W507726/1) for Shubham V. Kulkarni. We would also like to thank the Space Research Institute of the Russian Academy of Sciences (IKI), for scanning of the original plots for the Venera data sets and making them available.

References

Allen, D. A., & Crawford, J. W. (1984). Cloud structure on the dark side of Venus. *Nature*, *307*(5948), 222–224. https://doi.org/10.1038/307222a0

Arney, G., Meadows, V., Crisp, D., Schmidt, S. J., Bailey, J., & Robinson, T. (2014). Spatially resolved measurements of H_2O, HCl, CO, OCS, SO_2, cloud opacity, and acid concentration in the Venus near-infrared spectral windows. *Journal of Geophysical ResearchEducational Planning*, *119*(8), 1860–1891. https://doi.org/10.1002/2014JE004662

Avduevskij, V. S., Borodin, N. F., Burtsev, V. P., Malkov, Y. V., Marov, M. Y., Morozov, S. F., et al. (1976). Automatic stations Venera 9 and Venera 10—Operating of the reentry vehicles and measurement of the atmosphere's parameters. *KosIs*, *14*, 655–666.

Avduevsky, V. S., Marov, M. Y., Moshkin, B. E., & Ekonomov, A. P. (1973). Venera 8: Measurements of solar illumination through the atmosphere of Venus 1. *Journal of the Atmospheric Sciences*, *30*(6), 1215–1218. https://doi.org/10.1175/1520-0469(1973)030%3C1215:VMOSIT%3E2.0.CO;2

Ball, J. G., Reed, B. E., Grainger, R. G., Peters, D. M., Mather, T. A., & Pyle, D. M. (2015). Measurements of the complex refractive index of volcanic ash at 450, 546.7, and 650 nm. *Journal of Geophysical Research: Atmospheres*, *120*(15), 7747–7757. https://doi.org/10.1002/2015JD023521

Barstow, J. K., Tsang, C. C., Wilson, C. F., Irwin, P. G., Taylor, F. W., McGouldrick, K., et al. (2012). Models of the global cloud structure on Venus derived from Venus Express observations. *Icarus*, *217*(2), 542–560. https://doi.org/10.1016/j.icarus.2011.05.018

Bézard, B., De Bergh, C., Crisp, D., & Maillard, J. P. (1990). The deep atmosphere of Venus revealed by high-resolution nightside spectra. *Nature*, *345*(6275), 508–511. https://doi.org/10.1038/345508a0

Bézard, B., Tsang, C. C., Carlson, R. W., Piccioni, G., Marcq, E., & Drossart, P. (2009). Water vapor abundance near the surface of Venus from Venus Express/VIRTIS observations. *Journal of Geophysical Research*, *114*(5), 1–12. https://doi.org/10.1029/2008JE003251

Brackett, R. A., Fegley, B., & Arvidson, R. E. (1995). Volatile transport on Venus and implications for surface geochemistry and geology. *Journal of Geophysical Research*, *100*(E1), 1553–1563. https://doi.org/10.1029/94JE02708

Burch, D. E., Gryvnak, D. A., Patty, R. R., & Bartky, C. E. (1969). Absorption of infrared radiant Energy by CO_2 and H_2O IV shapes of collision-broadened CO_2 lines*. *Journal of the Optical Society of America*, *59*(3), 267. https://doi.org/10.1364/JOSA.59.000267

Carter, L. M., Gilmore, M. S., Ghail, R. C., Byrne, P. K., Smrekar, S. E., Ganey, T. M., & Izenberg, N. (2023). Sedimentary processes on Venus. *Space Science Reviews*, *219*(8), 1–25. https://doi.org/10.1007/s11214-023-01033-2

Ciesielski, A., Skowronski, L., Pacuski, W., & Szoplik, T. (2018). Permittivity of Ge, Te and Se thin films in the 200–1500 nm spectral range. Predicting the segregation effects in silver. *Materials Science in Semiconductor Processing*, *81*, 64–67. https://doi.org/10.1016/j.mssp.2018.03.003

Crisp, D. (1986). Radiative forcing of the Venus mesosphere. *Icarus*, *67*(3), 484–514. https://doi.org/10.1016/0019-1035(86)90126-0

Cutts, J., Baines, K., Dorsky, L., Frazier, W., Izraelevitz, J., Krishnamoorthy, S., et al. (2022). Exploring the clouds of Venus: Science driven aerobot missions to our sister planet. In *IEEE Aerospace Conference Proceedings, 2022-March*. https://doi.org/10.1109/AERO53065.2022.9843740

de Bergh, C., Bézard, B., Crisp, D., Maillard, J. P., Owen, T., Pollack, J., & Grinspoon, D. (1995). Water in the deep atmosphere of Venus from high-resolution spectra of the night side. *Advances in Space Research*, *15*(4), 79–88. https://doi.org/10.1016/0273-1177(94)00067-B

Deguine, A., Petitprez, D., Clarisse, L., Guđmundsson, S., Outes, V., Villarosa, G., & Herbin, H. (2020). Complex refractive index of volcanic ash aerosol in the infrared, visible, and ultraviolet. *Applied Optics*, *59*(4), 884. https://doi.org/10.1364/AO.59.000884

Dlugach, Z. M. (1988). The structure of the Venus atmosphere in accordance with Venera 11, 13, 14 optical measurements. *AVest*, *22*, 262–271.

Ekonomov, A. P., Moshkin, B. E., Golovin, I. M., Parfentev, N. A., & Sanko, N. F. (1979). Spectrophotometric experiment aboard the launched instruments of Venera 11 and Venera 12. 1. Method, results and preliminary analysis of measurements. *KosIs*, *17*, 714–726.

Ekonomov, A. P., Moshkin, B. E., Moroz, V. I., Golovin, I. M., Gnedykh, V. I., & Grigorev, A. V. (1983). *Experiment on UV-photometry aboard Venera 13 and Venera 14* (Vol. 21, pp. 254–268). KosIs.

Garvin, J. B., Getty, S. A., Arney, G. N., Johnson, N. M., Kohler, E., Schwer, K. O., et al. (2022). Revealing the mysteries of Venus: The DAVINCI mission. *The Planetary Science Journal*, *3*(5), 117. https://doi.org/10.3847/PSJ/AC63C2

Gilmore, M. S., Darby Dyar, M., Mueller, N., Brossier, J., Santos, A. R., Ivanov, M., et al. (2023). Mineralogy of the Venus surface. *Space Science Reviews*, *219*(7), 1–38. https://doi.org/10.1007/S11214-023-00988-6

Golovin, I. M., & Ustinov, E. A. (1982). Subcloud aerosol of the Venus atmosphere. *KosIs*, *20*, 104–110.

Golovin, Y. M. (1979). Optical properties of the Venus surface: Dependence of the albedo on wavelength. *KosIs*, *17*, 473–476.

Goody, R. M., & Yung, Y. L. (1989). *Atmospheric radiation: Theoretical basis*. Oxford University Press. https://doi.org/10.1093/oso/9780195051346.001.0001

Gordon, I. E., Rothman, L. S., Hargreaves, R. J., Hashemi, R., Karlovets, E. V., Skinner, F. M., et al. (2022). The HITRAN2020 molecular spectroscopic database. *Journal of Quantitative Spectroscopy and Radiative Transfer*, *277*, 107949. https://doi.org/10.1016/j.jqsrt.2021.107949

Grieger, B., Ignatiev, N. I., Hoekzema, N. M., & Keller, H. U. (2004). Indication of a near surface cloud layer on Venus from reanalysis of Venera 13/14 spectrophotometer data. In *European space agency, (special publication) esa sp* (pp. 63–70). ESA Publications Division.

Hahn, R. M., & Byrne, P. K. (2023). A morphological and spatial analysis of volcanoes on Venus. *Journal of Geophysical Research: Planets*, *128*(4). https://doi.org/10.1029/2023JE007753

Hansen, J. E., & Travis, L. D. (1974). Light scattering in planetary atmospheres. *Space Science Reviews*, *16*(4), 527–610. https://doi.org/10.1007/BF00168069

Haus, R., & Arnold, G. (2010). Radiative transfer in the atmosphere of Venus and application to surface emissivity retrieval from VIRTIS/VEX measurements. *Planetary and Space Science*, *58*(12), 1578–1598. https://doi.org/10.1016/j.pss.2010.08.001

Herrick, R. R., Bjonnes, E. T., Carter, L. M., Gerya, T., Ghail, R. C., Gillmann, C., et al. (2023). Resurfacing history and volcanic activity of Venus. *Space Science Reviews*, *219*(4), 1–32. https://doi.org/10.1007/S11214-023-00966-Y

Herrick, R. R., & Hensley, S. (2023). Surface changes observed on a Venusian volcano during the Magellan mission. *Science*, *379*(6638), 1205–1208. https://doi.org/10.1126/science.abm7735

Howard, J. N., Burch, D. E., & Williams, D. (1956). Infrared transmission of synthetic atmospheres* II absorption by carbon dioxide. *Journal of the Optical Society of America*, *46*(4), 237. https://doi.org/10.1364/josa.46.000237

Hunten, D. M., Colin, L., Donahue, T. M., & Moroz, V. I. (1983). Venus.

Ignatiev, N., & Kulkarni, S. V. (2024). Radiation in the atmosphere of Venus measured in the spectrophotometric expertiment onboard the Venera-13 descent probe [Dataset]. *Mendeley*. https://doi.org/10.17632/93wzfnksc6.1

Ignatiev, N. I., Moroz, V. I., Moshkin, B. E., Ekonomov, A. P., Gnedykh, V. I., Grigor'ev, A. V., & Khatuntsev, I. V. (1997). Water vapor in the lower atmosphere of Venus: New analysis of the optical spectra measured by entry probes. *Cosmic Research*, *35*(1), 1–14.

Irwin, P., Wilson, C., Alday, J., Roos-Serote, M., Barstow, J., & Aslam, S. (2020). *Modelling the in situ solar and thermal radiation environment for future entry probe missions to Venus* (pp. 2020–2312). EPSC. https://doi.org/10.5194/EPSC2020-312

Irwin, P. G. J., Teanby, N. A., de Kok, R., Fletcher, L. N., Howett, C. J., Tsang, C. C., et al. (2008). The NEMESIS planetary atmosphere radiative transfer and retrieval tool. *Journal of Quantitative Spectroscopy and Radiative Transfer*, *109*(6), 1136–1150. https://doi.org/10.1016/j.jqsrt.2007.11.006

Irwin, P. G. J., Teanby, N. A., de Kok, R., Fletcher, L. N., Howett, C. J. A., Tsang, C. C. C., et al. (2022a). Nemesis [Software]. *Zenodo*. https://doi.org/10.5281/zenodo.5816714

Irwin, P. G. J., Teanby, N. A., de Kok, R., Fletcher, L. N., Howett, C. J. A., Tsang, C. C. C., et al. (2022b). Nemesis documentation [Software Documentation]. *Zenodo*. https://doi.org/10.5281/zenodo.5816723

James, E. P., Toon, O. B., & Schubert, G. (1997). A numerical microphysical model of the condensational Venus cloud. *Icarus*, *129*(1), 147–171. https://doi.org/10.1006/icar.1997.5763

Klose, K. B., Wood, J. A., & Hashimoto, A. (1992). Mineral equilibria and the high radar reflectivity of Venus mountaintops. *Journal of Geophysical Research*, *97*(E10), 16353–16369. https://doi.org/10.1029/92je01865

Knollenberg, R. G., & Hunten, D. M. (1980). The microphysics of the clouds of Venus: Results of the Pioneer Venus particle size spectrometer experiment. *Journal of Geophysical Research*, *85*(A13), 8039–8058. https://doi.org/10.1029/ja085ia13p08039

Kohler, E., Johnson, N. M., Kohler, E., & Johnson, N. M. (2015). Current Laboratory Research and Venus in-situ Chamber investigations. *LPICo*, *1838*, 4019.

Kreslavsly, M. A., & Bondarenko, N. V. (2017). *Aeolian sand transport and Aeolian deposits on Venus: A review* (Vol. 26, pp. 29–46). Elsevier B. V. https://doi.org/10.1016/j.aeolia.2016.06.001

Kulkarni, S. V., Irwin, P. G. J., Wilson, C. F., & Ignatiev, N. (2024). Data associated with manuscript tilted a search for the near-surface particulate layer using Venera 13 in situ spectroscopic observations [Dataset]. *Zenodo*. https://doi.org/10.5281/zenodo.14850879

Lebonnois, S., & Schubert, G. (2017). The deep atmosphere of Venus and the possible role of density-driven separation of CO_2 and N_2. *Nature Geoscience*, *10*(7), 473–477. https://doi.org/10.1038/ngeo2971

Lefèvre, M. (2022). Venus boundary layer dynamics: Eolian transport and convective vortex. *Icarus*, *387*, 115167. https://doi.org/10.1016/j.icarus.2022.115167

Limaye, S. S., Grassi, D., Mahieux, A., Migliorini, A., Tellmann, S., & Titov, D. (2018). Venus atmospheric thermal structure and radiative balance. *Author*, *214*(5), 102. https://doi.org/10.1007/s11214-018-0525-2

Mahmoud, S., Eid, A. H., & Omar, H. (1997). Optical characteristics of bismuth sulfide (Bi2S3) thin films. *Fizika A : Journal of Experimental and Theoretical Physics*, *6*(3), 111–120.

Manzanares, C., I., Muñoz, A., & Hidalgo, D. (1984). Collision-induced absorption of infrared radiation by N_2, O_2 and CO_2. *Chemical Physics*, *87*(3), 363–371. https://doi.org/10.1016/0301-0104(84)85117-4

Marcq, E., Mills, F. P., Parkinson, C. D., & Vandaele, A. C. (2018). Composition and chemistry of the neutral atmosphere of Venus. *Space Science Reviews*, *214*(1), 10. https://doi.org/10.1007/s11214-017-0438-5

Marin, F., Rohatgi, A., & Charlot, S. (2017). WebPlotDigitizer, a polyvalent and free software to extract spectra from old astronomical publications: Application to ultraviolet spectropolarimetry. arXiv: Instrumentation and Methods for Astrophysics.

Marov, M. I., Byvshev, B. V., Baranov, B. P., Lebedev, V. N., Lukashevich, N. L., Maksimov, A. V., et al. (1983). *Investigation of the structure of Venus clouds with nephelometers aboard Venera 13 and Venera 14* (Vol. 21, pp. 269–278). KosIs.

Marov, M. I., Byvshev, B. V., Baranov, I. P., Lebedev, V. N., Lystsev, V. E., Maksimov, A. V., et al. (1979). The aerosol component in the Venus atmosphere from data of measurements aboard the Venera 11 station. *KosIs*, *17*, 743–746.

Mico, S., Deda, A., Tsaousi, E., Alushllari, M., & Pomonis, P. (2019). Complex refractive index of aerosol samples. In *Aip conference proceedings* (Vol. 2109, p. 060002). American Institute of Physics Inc. https://doi.org/10.1063/1.5110120

Moshkin, B. E., Ekonomov, A. P., Moroz, V. I., Gelovin, I. M., Gnedykh, V. I., Grigorev, A. V., & Diachkov, A. V. (1983). Spectrophotometric experiment aboard the Venera 13 and Venera 14 apparatuses. 1. Method, results and preliminary analysis of measurements. *Kosmicheskie Issledovaniia*, *21*, 236–245.

Mueller, N. T., Smrekar, S. E., & Tsang, C. C. (2020). Multispectral surface emissivity from VIRTIS on Venus Express. *Icarus*, *335*(August 2019), 113400. https://doi.org/10.1016/j.icarus.2019.113400

O'Rourke, J. G., Wilson, C. F., Borrelli, M. E., Byrne, P. K., Dumoulin, C., Ghail, R., et al. (2023). Venus, the Planet: Introduction to the evolution of Earth's sister planet. *Space Science Reviews*, *219*(1), 1–61. https://doi.org/10.1007/S11214-023-00956-0

Palmer, K. F., & Williams, D. (1975). Optical constants of sulfuric acid; application to the clouds of Venus? *Applied Optics*, *14*(1), 208. https://doi.org/10.1364/ao.14.000208

Perevalov, V. I., & Tashkun, S. A. (2008). CDSD-296 (carbon dioxide spectroscopic databank): Updated and enlarged version for atmospheric applications. In *The 10th hitran database conference, harvard-smithsonian center for astrophysics*. https://doi.org/10.5281/zenodo.17520

Pettengill, G. H., Ford, P. G., & Simpson, R. A. (1996). Electrical properties of the Venus surface from bistatic radar observations. *Science*, *272*(5268), 1628–1631. https://doi.org/10.1126/SCIENCE.272.5268.1628

Pettengill, G. H., Wilt, R. J., & Ford, P. G. (1992). Dielectric surface properties of Venus. *LPICo*, *789*, 88.

Plass, G. N., Kattawar, G. W., & Catchings, F. E. (1973). Matrix operator theory of radiative transfer. 1: Rayleigh scattering. *Applied Optics*, *12*(2), 314–329. https://doi.org/10.1364/AO.12.000314

Pollack, J. B., Dalton, J. B., Grinspoon, D., Wattson, R. B., Freedman, R., Crisp, D., et al. (1993). Near-infrared light from Venus'. *Nightside: A Spectroscopic Analysis*, *103*(1), 1–42. https://doi.org/10.1006/icar.1993.1055

Pollack, J. B., Toon, O. B., & Khare, B. N. (1973). Optical properties of some terrestrial rocks and glasses. *Icarus*, *19*(3), 372–389. https://doi.org/10.1016/0019-1035(73)90115-2

Ragent, B., & Blamont, J. (1980). The structure of the clouds of Venus: Results of the Pioneer Venus nephelometer experiment. *Journal of Geophysical Research*, *85*(A13), 8089–8105. https://doi.org/10.1029/JA085IA13P08089

Ragent, B., Wong, T., Blamont, J. E., Eskovitz, A. J., Harnett, L. N., & Pallai, A. (1980). Pioneer Venus sounder and small probes nephelometer instrument. *IEEE Transactions on Geoscience and Remote Sensing, GE*, *18*(1), 111–117. https://doi.org/10.1109/TGRS.1980.350292

Rastogi, P., Chu, A., Dang, T. H., Prado, Y., Gréboval, C., Qu, J., et al. (2021). Complex optical index of HgTe nanocrystal infrared thin films and its use for short wave infrared photodiode design. *Advanced Optical Materials*, *9*(10), 2002066. https://doi.org/10.1002/ADOM.202002066

Ravindra, N. M., & Srivastava, V. K. (1982). Experimental studies of some opto-electronic properties of thin films of galena. *Infrared Physics*, *22*(2), 81–89. https://doi.org/10.1016/0020-0891(82)90022-7

Reed, B. E., Peters, D. M., McPheat, R., & Grainger, R. G. (2018). The complex refractive index of volcanic ash aerosol retrieved from spectral mass extinction. *Journal of Geophysical Research: Atmospheres*, *123*(2), 1339–1350. https://doi.org/10.1002/2017JD027362

Rodgers, C. D. (2000). Inverse methods for atmospheric sounding. *World Scientific*, *2*. https://doi.org/10.1142/3171

Rothman, L. S., Gordon, I. E., Barber, R. J., Dothe, H., Gamache, R. R., Goldman, A., et al. (2010). HITEMP, the high-temperature molecular spectroscopic database. *Journal of Quantitative Spectroscopy and Radiative Transfer*, *111*(15), 2139–2150. https://doi.org/10.1016/j.jqsrt.2010.05.001

Rothman, L. S., Wattson, R. B., Gamache, R., Schroeder, J. W., & McCann, A. (1995). HITRAN HAWKS and HITEMP: High-temperature molecular database. *Atmospheric Propagation and Remote Sensing IV*, *2471*(June 1995), 105–111. https://doi.org/10.1117/12.211919

Sagdeev, R. Z., & Moroz, V. I. (1982). Venera 13 and Venera 14. *Soviet Astronomy Letters*, *8*, 209–211.

Schaefer, L., & Fegley, B. (2004). Heavy metal frost on Venus. *Icarus*, *168*(1), 215–219. https://doi.org/10.1016/J.ICARUS.2003.11.023

Schiffer, R. A., Beck, A. J., Aeronautics, U. S. N., & Administration, S. (1968). *Models of Venus atmosphere*. National Aeronautics and Space Administration.

Seiff, A., Schofield, J. T., Kliore, A. J., Taylor, F. W., Limaye, S. S., Revercomb, H. E., et al. (1985). Models of the structure of the atmosphere of Venus from the surface to 100 kilometers altitude. *Advances in Space Research*, *5*(11), 3–58. https://doi.org/10.1016/0273-1177(85)90197-8

Smrekar, S., Dyar, D., Helbert, J., Hensley, S., Nunes, D., & Whitten, J. (2020). VERITAS (Venus emissivity, Radio Science, InSAR, topography and spectroscopy): A proposed discovery mission. EPSC2020. https://doi.org/10.5194/EPSC2020-447

Smrekar, S. E., Stofan, E. R., Mueller, N., Treiman, A., Elkins-Tanton, L., Helbert, J., et al. (2010). Recent hotspot volcanism on Venus from VIRTIS emissivity data. *Science*, *328*(5978), 605–608. https://doi.org/10.1126/SCIENCE.1186785/SUPPL{_}FILE/PAPV3.PDF

Snels, M., Stefani, S., Grassi, D., Piccioni, G., & Adriani, A. (2014). Carbon dioxide opacity of the Venus' atmosphere. *Planetary and Space Science*, *103*, 347–354. https://doi.org/10.1016/J.PSS.2014.08.002

Straume-Lindner, A.-G., Buchwald, R., Crouzet, P.-E., Titov, D., Voirin, T., & Wielders, A. (2022). EnVision: An ESA Medium-class mission to Venus in collaboration with NASA. EPSC2022. https://doi.org/10.5194/EPSC2022-196

Suomi, V. E., Sromovsky, L. A., & Revercomb, H. E. (1979). Preliminary results of the Pioneer Venus small probe net flux radiometer experiment. *Science*, *205*(4401), 82–85. https://doi.org/10.1126/SCIENCE.205.4401.82

Taylor, F. W. (2006). Venus before Venus Express. *Planetary and Space Science*, *54*(13–14), 1249–1262. https://doi.org/10.1016/j.pss.2006.04.031

Thomas, J. C. (1987). The determination of log normal particle size distributions by dynamic light scattering. *Journal of Colloid and Interface Science*, *117*(1), 187–192. https://doi.org/10.1016/0021-9797(87)90182-2

Titov, D. V., Ignatiev, N. I., McGouldrick, K., Wilquet, V., & Wilson, C. F. (2018). Clouds and hazes of Venus. *Author*, *214*(8), 126. https://doi.org/10.1007/s11214-018-0552-z

Tonkov, M. V., Filippov, N. N., Bertsev, V. V., Bouanich, J. P., Van-Thanh, N., Brodbeck, C., et al. (1996). Measurements and empirical modeling of pure CO_2 absorption in the 23-μm region at room temperature: Far wings, allowed and collision-induced bands. *Applied Optics*, *35*(24), 4863. https://doi.org/10.1364/ao.35.004863

Tsang, C. C. C., Irwin, P. G. J., Taylor, F. W., & Wilson, C. F. (2008). A correlated-k model of radiative transfer in the near-infrared windows of Venus. *Journal of Quantitative Spectroscopy and Radiative Transfer*, *109*(6), 1118–1135. https://doi.org/10.1016/j.jqsrt.2007.12.008

Wilson, C. F., Marcq, E., Gillmann, C., Widemann, T., Korablev, O., Mueller, N. T., et al. (2024). Possible effects of volcanic eruptions on the modern atmosphere of Venus. *Space Science Reviews*, *220*(3), 31. https://doi.org/10.1007/s11214-024-01054-5